

A STUDY OF THE DESIGN OF ADAPTIVE CAMBER WINGLETS

A Thesis

presented to

the Faculty of California Polytechnic State University,

San Luis Obispo

In Partial Fulfillment

of the Requirements for the Degree

Master of Science in Aerospace Engineering

by

Justin Rosescu

June 2020

© 2020

Justin Julian Rosescu

ALL RIGHTS RESERVED

COMMITTEE MEMBERSHIP

TITLE: A Study of the Design of Adaptive Camber
Winglets

AUTHOR: Justin Rosescu

DATE SUBMITTED: June 2020

COMMITTEE CHAIR: Paulo Iscold, Ph.D.
Professor of Aerospace Engineering

COMMITTEE MEMBER: David Marshall, Ph.D.
Professor of Aerospace Engineering

COMMITTEE MEMBER: Aaron Drake, Ph.D.
Professor of Aerospace Engineering

COMMITTEE MEMBER: Kurt Colvin, Ph.D.
Professor of Industrial Engineering

ABSTRACT

A Study of the Design of Adaptive Camber Winglets

Justin Julian Rosescu

A numerical study was conducted to determine the effect of changing the camber of a winglet on the efficiency of a wing in two distinct flight conditions. Camber was altered via a simple plain flap deflection in the winglet, which produced a constant camber change over the winglet span. Hinge points were located at 20%, 50% and 80% of the chord and the trailing edge was deflected between -5° and $+5^\circ$. Analysis was performed using a combination of three-dimensional vortex lattice method and two-dimensional panel method to obtain aerodynamic forces for the entire wing, based on different winglet camber configurations. This method was validated against high-fidelity steady Reynolds Averaged Navier-Stokes simulations to determine the accuracy of these methods. It was determined that any winglet flap deflections increased induced drag and parasitic drag, thus decreasing efficiency for steady level flight conditions. Positive winglet flap deflection at higher lift conditions may increase efficiency, but the validity of the vortex lattice method results for these conditions are dubious. A high-fidelity method should be used for the high lift condition to obtain accurate efficiency data.

ACKNOWLEDGMENTS

I would like to thank all my professors for providing so much knowledge over the years. I would like to specially thank Dr. Iscold for providing deep insight and keeping me on the right track through the course of this thesis. Your timely and detailed responses to my questions were invaluable for my endeavors with this thesis, and I am honored to have worked with you.

Thank you to all my friends who have supported me throughout the years and kept me sane. All of my graduate and undergraduate friends have helped to smooth over the bumpy parts of my academic career and helped make this journey more surmountable. I would have gone crazy early in my undergraduate studies were it not for you lot, and for that I thank you.

Lastly, I would like to thank my family for supporting me and raising me up to reach new heights. Thank you, Mom for showing immense strength to overcome some of the most challenging experiences anyone would ever have to deal with, and this inspiring me to overcome my own challenges. Thank you, Dad for helping me with all the little problems that come with life and helping me transition to a responsible adult. Thank you, Nick for setting an example of how to enjoy higher education while making the most of your time in university. And thank you Nina for seeing me off at the beginning of this journey. Your love and support still keep me going even to this day. I love you all.

TABLE OF CONTENTS

	Page
LIST OF TABLES	vii
LIST OF FIGURES.....	viii
NOMENCLATURE.....	x
CHAPTER	
1. INTRODUCTION	1
1.1 Effect of Winglets on Induced Drag	1
1.2 Effect of Winglets on Parasitic Drag	2
1.3 Effect of Camber	2
1.4 Project Objective	4
2. LITERATURE REVIEW	5
2.1 Winglet Analysis and Simulation.....	5
2.2 Morphing Wing.....	6
2.3 Adjustable Camber Winglets.....	7
3. METHODOLOGY	8
3.1 Description of Geometry	8
3.2 Determination of Flight Conditions	11
3.3 VLM Analysis.....	12
3.3.1 Calculation of Aerodynamic Forces for VLM.....	12
3.3.2 Cambered Winglet Analysis.....	16
3.3.3 Panel Method Convergence Study	18
3.3.4 Vortex Lattice Method Convergence Study	20
3.4 RANS Analysis.....	23
3.4.1 Description of RANS Geometry.....	24
3.4.2 Calculation of Aerodynamic Forces for RANS	25
3.4.3 RANS Flow Characteristics	26
3.4.4 RANS Mesh Convergence Study	27
3.5 Comparison of Methods.....	32
4. RESULTS.....	34
4.1 RANS Validation of VLM Results	34
4.1.1 Lift Validation	34
4.1.2 Drag Validation.....	35
4.1.2.1 Induced Drag Validation.....	35
4.1.2.2 Parasitic Drag Validation	35
4.1.2.3 Total Drag Validation.....	36
4.2 Winglet Camber Analysis.....	37
4.2.1 Camber Effects on Airfoil Drag.....	37
4.2.2 Camber Effects on Wing Induced Drag.....	39
4.2.3 Camber Effects on Wing Total Drag.....	39
4.3 8g Turn Efficiency	41
4.4 Steady Level Flight Efficiency	45
5. CONCLUSION	49
6. FUTURE WORK.....	50
REFERENCES	51
APPENDIX	54

LIST OF TABLES

Table	Page
3.1 Flight Conditions for Steady Level Flight and 8g Turn.....	12
3.2 Continuum and Reference Settings	26
3.3 Mesh Settings	27
3.4 Total Cell Count.....	30
3.5a Domain Size Lift Comparison.....	32
3.5b Domain Size Drag Comparison.....	32
A1 Airfoil Coordinates	54

LIST OF FIGURES

Figure	Page
1.1 Illustration of Induced Drag.....	2
1.2 Effect of Camber on Zero-lift Angle	3
1.3 Parabolic Drag Polar.....	3
1.4 Extra Edge 540 Aircraft	4
2.1 Effect of Winglet on Spanwise Lift Distribution.....	5
3.1a Initial Geometry with Winglets	9
3.1b Wing Planform View	9
3.1c Winglet View	9
3.2a Wing Airfoils.....	10
3.2b Winglet Airfoils	10
3.3 Vortex Lattice Model	11
3.4 Transition Criterion.....	14
3.5 Location of Forced Transition on the Wing.....	14
3.6 Winglet Configuration Convention	17
3.7 Distribution of Airfoil Panels.....	18
3.8 Panel Method Convergence Study	19
3.9 VLM Spanwise Wing Convergence.....	21
3.10 VLM Chordwise Wing Convergence.....	22
3.11 VLM Spanwise Winglet Convergence.....	23
3.12 RANS Domain, $c = 1.6m$ Root Chord Length	25
3.13 RANS Induced Drag Versus Trefftz Plane Location	26

3.14	Near-wing Cell Aspect Ratio	28
3.15	Flow Velocity for Base Domain Size.....	29
3.16	5 m Base Size, 100-Chord Length Domain Residuals.....	31
3.17	5 m Base Size, 50-Chord Length Domain Residuals	32
4.1	VLM Versus RANS Lift Comparison.....	34
4.2	VLM Versus RANS Induced Drag Comparison.....	35
4.3	VLM Versus RANS Parasitic Drag Comparison.....	36
4.4	VLM Versus RANS Total Drag Comparison.....	37
4.5	Winglet Base Airfoil Parasitic Drag Polar	38
4.6	Winglet Top Airfoil Parasitic Drag Polar.....	38
4.7	Effect of Winglet Flap Deflection on Induced Drag.....	39
4.8	Effect of Winglet Flap Deflection on Total Drag.....	40
4.9	Effect of Winglet Flap Deflection on Efficiency.....	41
4.10	Effect of Winglet Camber at High g Turn	42
4.11	Effect of Winglet Flap Deflection on Lift Distribution, High g Condition	43
4.12	Effect of Winglet Flap Deflection on Induced Drag Distribution, High g Condition.....	43
4.13	Effect of Winglet Flap Deflection on Parasitic Drag Distribution, High g Condition	44
4.14	Effect of Winglet Flap Deflection on Total Drag Distribution, High g Condition.....	44
4.15	Effect of Winglet Camber at Low g Steady Level Flight	45
4.16	Effect of Winglet Flap Deflection on Lift Distribution, Low g Condition.....	46
4.17	Effect of Winglet Flap Deflection on Induced Drag Distribution, Low g Condition	46
4.18	Effect of Winglet Flap Deflection on Parasitic Drag Distribution, Low g Condition.....	47
4.19	Effect of Winglet Flap Deflection on Total Drag Distribution, Low g Condition	48

NOMENCLATURE

C_D	Drag Coefficient
C_d	Airfoil Drag Coefficient
C_L	Lift Coefficient
C_l	Airfoil Lift Coefficient
D	Drag
D_i	Induced Drag
E	Efficiency
F	Force
L	Lift
N	Amplification Factor Threshold
Re	Reynolds Number
S	Wing Area
b	Wingspan
c	Chord Length
g	Load Factor
k, T_{ke}	Turbulent Kinetic Energy
kg	Kilogram
m	Meter
n_f	Force Direction Vector
s	Second
u_∞	Freestream Velocity
v	Velocity in y-direction
w	Velocity in z-direction
α	Angle of Attack

δ	Percentual
ε, Tdr	Turbulent Dissipation Rate
ν	Kinematic Viscosity
ρ_{∞}	Freestream Air Density
σ	Boundary Layer Thickness
θ	Momentum Thickness

Chapter 1

INTRODUCTION

Winglets are vertical extensions attached to the wing tips of aircraft that are typically used to reduce drag at lifting conditions. This leads to an increase in span-wise efficiency compared to a wing with no winglets, but as a tradeoff, they always increase the parasitic drag of the wing. Winglets seem to be advantageous for high-lift conditions like climbing and turning, however, they may decrease efficiency for lower-lift conditions like high speed dash [1], as a result of the winglets' separate effect on the lift-induced drag and parasitic drag of the wing.

1.1 Effect of Winglets on Induced Drag

Induced drag is the drag due to the lift generated by a finite wing. As shown in Figure 1.1, on a specific section of a finite wing at a given angle of attack, the resultant lift vector of an airfoil has a component in the freestream direction. This effect is due to the fact that a finite wing has a wingtip vortex, which induce downward momentum α_i along the span, lowering the wing's effective angle of attack α_{eff} . Since the total lift of the wing should be measured, by definition, perpendicular to the incoming flow, all these streamwise components should sum to the drag force, in this case, the induced drag. Winglets counter this by reducing the strength of the wingtip vortex, which reduces the induced drag.

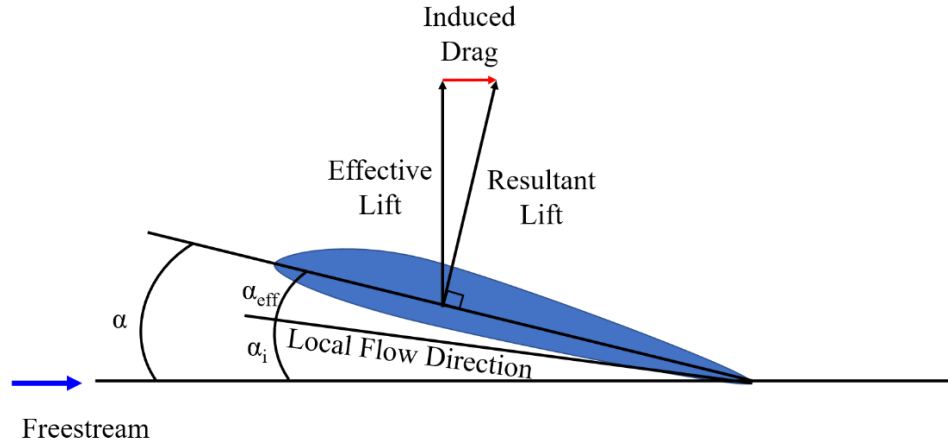


Figure 1.1: Illustration of Induced Drag

Induced drag is proportional to the square of the lift produced by the wing. At higher lift conditions like climbing and turning, the induced drag is substantial. Winglets' effectiveness at reducing this induced drag is more noticeable for these conditions. However, at lower lift conditions like cruise, there is less lift being produced and therefore less induced drag, diminishing the performance gains of winglets.

1.2 Effect of Winglets on Parasitic Drag

Parasitic drag for wings refers drag due to the predominantly viscous forces, where the more surface area that is exposed to fluid flow, the more parasitic drag is produced. Since winglets increase the wetted area of wings, they will produce more parasitic drag compared to a wing without winglets. Although winglets produce slightly less induced drag at low lift conditions, this does not account for their comparatively larger increase in parasitic drag, which is why winglets are less efficient at these conditions.

1.3 Effect of Camber

Changing the camber of an airfoil will change its zero-lift angle of attack α_0 such that a cambered airfoil can produce the same amount of lift, but at a smaller angle of attack compared to an airfoil with less camber, as shown in Figure 1.2. As shown in Figure 1.3, drag has a roughly

parabolic relation with increasing angle of attack, so a cambered airfoil should be able to produce less drag for a given amount of lift since it needs a lower angle of attack to produce this lift.

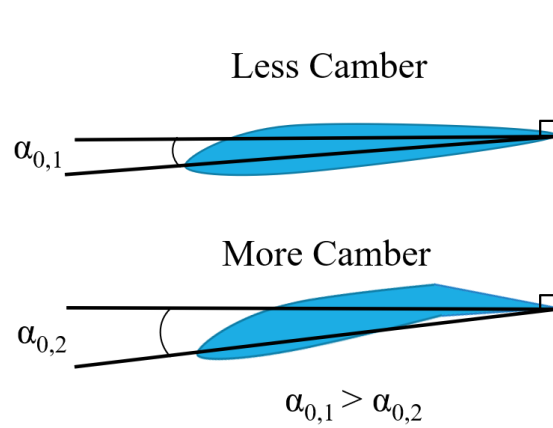


Figure 1.2: Effect of Camber on Zero-lift Angle

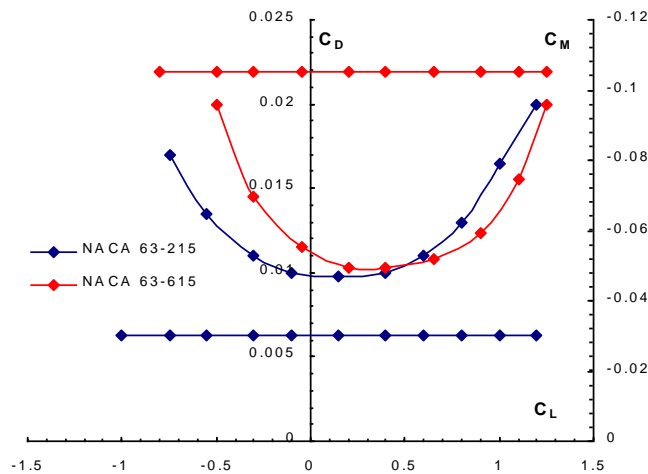


Figure 1.3: Parabolic Drag Polar

Decreasing winglet camber at high speeds should decrease the amount of lift produced by the winglet, such that it should be at minimum drag conditions and thus have the effect of minimizing drag due to the winglets. At lower speeds and higher lift conditions, increasing winglet camber should increase the lift produced by the winglet, spreading the lift distribution of the wing towards the wingtip. This enables the wing to fly at a lower angle of attack since the winglets take more of the lifting load, which should reduce the drag of the main wing.

1.4 Project Objective

The objective of this thesis is to determine the effect of a variable-camber winglets on its overall efficiency, when applied to an Extra Edge 540 acrobatic race aircraft, seen in Figure 1.4 [2]. In this particular case, the goal is to minimize drag in two distinct flight conditions: i) a high lift condition based on an 8g turn at 200 knots and ii) low lift condition based on steady level flight at 200 knots. The geometry is a trapezoidal wing with winglets that were, originally, designed to minimize induced drag at high lift conditions and minimize parasitic drag at low lift conditions, and thus minimize race times for typical circuits. To achieve this goal, numerical analysis was performed on the three-dimensional CAD model of this wing. Camber changes to the winglet were made by introducing a simple plain flap at different locations along the chord of the winglet. Two numerical analysis techniques were used: i) a low-fidelity vortex lattice method (VLM) that allowed easy manipulation of winglet camber, but required separate calculation of induced and parasitic drag, and ii) a high-fidelity Reynolds Averaged Navier-Stokes method that calculated all aerodynamic forces within the same software suite but required use of computer aided design (CAD) to make camber changes.



Figure 1.4: Extra Edge 540 Aircraft

2.1 Winglet Analysis and Simulation

Winglet may be analyzed experimentally to obtain realistic aerodynamic forces. Through wind tunnel testing, it was discovered that winglets can provide the same increase in efficiency as horizontal wing extensions [3]. In addition, it has been shown that winglets increase the spanwise loading of an aircraft's wing, as shown in Figure 2.1 [4]. This conclusion is the basis from which winglets are implemented on aircraft that need an increase in efficiency for high lift conditions.

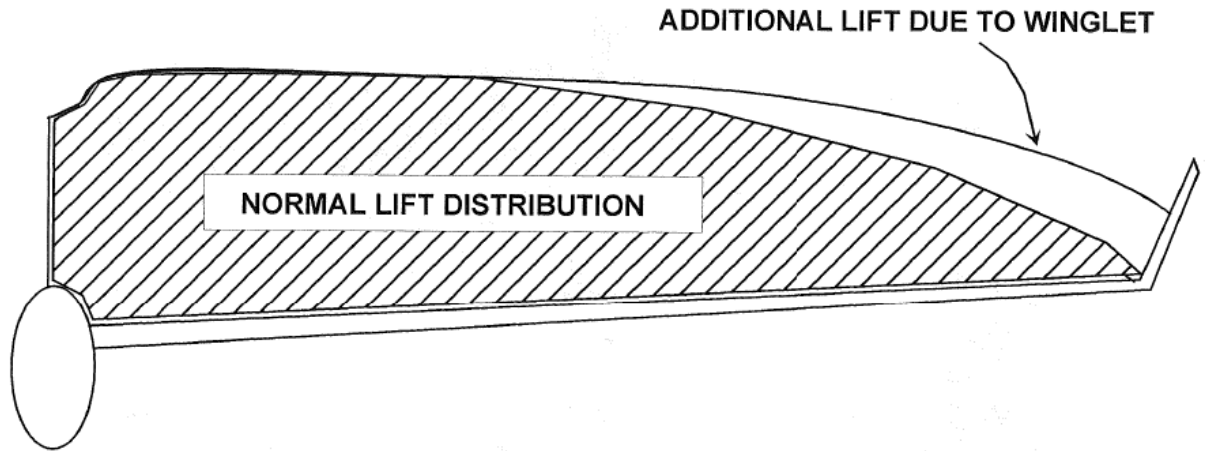


Figure 2.1: Effect of Winglet on Spanwise Lift Distribution

While wind tunnel and flight tests may be a robust way for obtaining accurate performance predictions for winglet configurations, the process for manufacturing the test articles and performing these tests are costly and require much time to accomplish. Compared to experimental testing, numerical analysis in the form of VLM and RANS provide a relatively cheaper and quicker alternative. VLM can be used to quickly analyze the aerodynamic forces of a multitude of winglet configurations, allowing easy alteration to winglet span, dihedral angle, sweep, and taper ratio to find an optimal design for a specific flight condition [5].

VLM is a low-fidelity method that is mainly used in preliminary design to calculate induced drag of a wing through use of integrating the radial velocity of a far-field Trefftz plane, of which the methodology will be explained in Chapter 3. It should be noted that VLM cannot calculate parasitic drag or interference drag due to complex model geometry. Other methods should be used to obtain these forces for preliminary design [6], but a more robust method like RANS that calculates all of these forces should be used to obtain accurate performance predictions [7,8].

2.2 Morphing Wing

Recently, the use of morphing wings and adaptive geometry has gained the interest of researchers as an alternative to optimize a flying vehicle for different flight conditions. Research has already been done on the feasibility of different physical actuation systems and materials by using finite element analysis and experimental testing to determine stresses seen in the physical configuration of a morphing wing or winglet [9, 10] showing promise for future implementation of these technologies in aircraft. These studies in product development enables other researchers to develop an optimal design for a wing shape based on more than one flight condition, since mechanisms for changing the shape between two or more configurations is being researched in tandem.

Numerical analysis through use of VLM and RANS has shown that a wing shape that has been designed to be most efficient for one flight condition can increase efficiency for other flight conditions through use of adaptive wing twist [11] and wing camber changes localized to the trailing edge of the wing [12]. This latter example is important since it proved that only optimizing the shape of the trailing edge of a wing can produce a similar gain in efficiency to a wing whose full planform shape has been optimized. This serves as the basis for changing the camber of a winglet to increase efficiency by only deflecting a trailing edge flap, as opposed to altering the leading-edge shape or twist angle.

2.3 Adjustable Camber Winglets

With the research being done on creating adaptive geometry to optimize wing shapes for different flight conditions, some of these concepts carried over to determine the effect of changing the camber for winglets based on different flight conditions. However, early attempts at researching the effects of winglet camber were not promising, as researchers have found through wind tunnel experiments that any adjustment in winglet camber by using a simple plain flap at low lift flight conditions decreased efficiency over an otherwise optimized winglet [13]. The researchers admitted to limitations in their methodology as only the wing tip with winglet was tested as opposed to a full wing, so there still remains room for further analysis. A more recent study has modeled a full aircraft with adaptive camber winglets using computational fluid dynamics (CFD) and came to the same conclusion, however this study used winglet flap extensions at the trailing edge as opposed to changing the camber of a preexisting winglet [14]. While this result agrees with the notion that changing camber is detrimental to wing performance, the methodology and model setup introduced another variable in the form of winglet extension size that may adversely affect results compared to a winglet with unaltered size.

A promising foundation for using adaptive camber to optimize a winglet for different flight conditions came in the form of a numerical study using a full potential equation solver coupled with three-dimensional boundary layer modelling to determine the effects of changing winglet camber to improve efficiency of a mission-optimized winglet [15]. This study found that through changing the leading and trailing edge geometry of the winglet, up to a 0.58% reduction in drag may be obtained for a flight condition of which original winglet was not optimized. While this study made use of both the leading and trailing edge to adjust winglet camber, the previous study that showed that a trailing edge morphing wing can produce a similar efficiency gain as a full-body morphing system provides the basis from which a simpler plain flap adaptive camber winglet can produce these performance gains.

Chapter 3

METHODOLOGY

Two methods were used to determine the aerodynamic characteristics of winglet performance for this study. The first stage involved the use of a low-fidelity three-dimensional vortex lattice method (VLM) to determine winglet's camber effects on lift and drag for the entire wing. This method focused on analyzing the aerodynamic characteristics of multiple winglet camber configurations. The second method used steady Reynolds Averaged Navier-Stokes (RANS) simulations to model the air flow in a discretized domain and obtain aerodynamic forces via the pressure and shear stresses caused by the flow on the wing's surface. Compared to VLM, RANS is more computationally expensive.

While RANS can generate a solution to the flow field over a body that is more accurate to reality than VLM, the computation time needed to simulate all the winglet configurations would significantly extend the timeline of this study [16]. If it can be proven that a lower-fidelity and computationally cheaper method like VLM can provide results as accurate as this high-fidelity computationally expensive method like RANS, then this lower-fidelity method can be used to design and analyze these winglets.

3.1 Description of Geometry

The geometry being used for this experiment is based on the wing for the Edge 540 acrobatic race plane. Figure 3.1a shows the starting geometry, complete with outlines for control surfaces. This is a simple trapezoidal wing with a symmetrical airfoil shape throughout the wingspan, and cambered airfoils for the winglets with geometric twist between the base and top of the winglet. The locations of these airfoils are shown in Figures 3.1b and 3.1c, and their shape are described in Figures 3.2a and 3.2b.

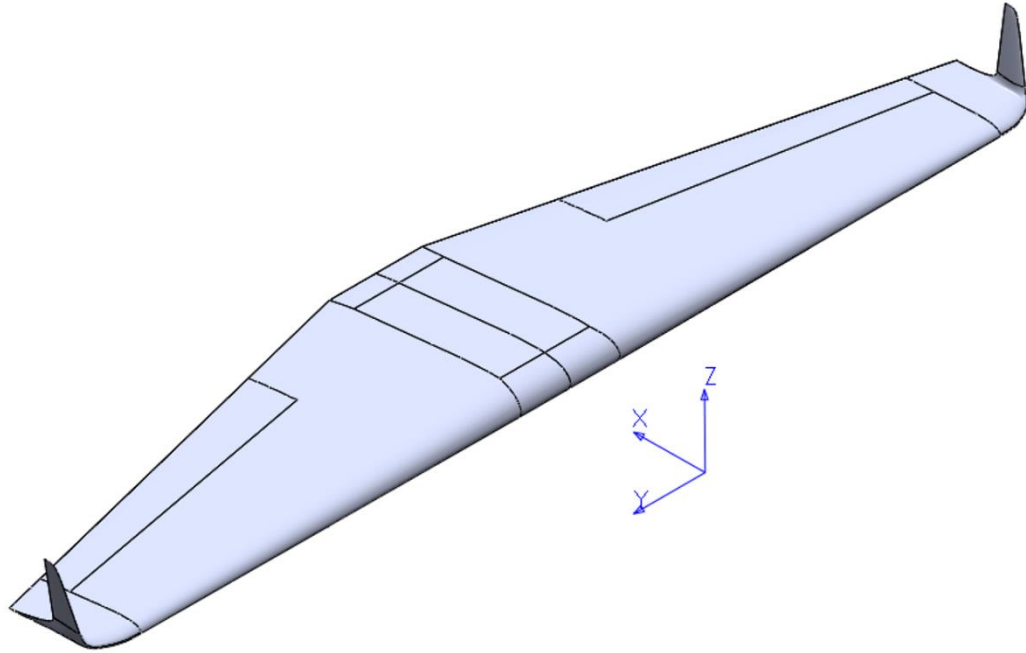


Figure 3.1a: Initial Geometry with Winglets

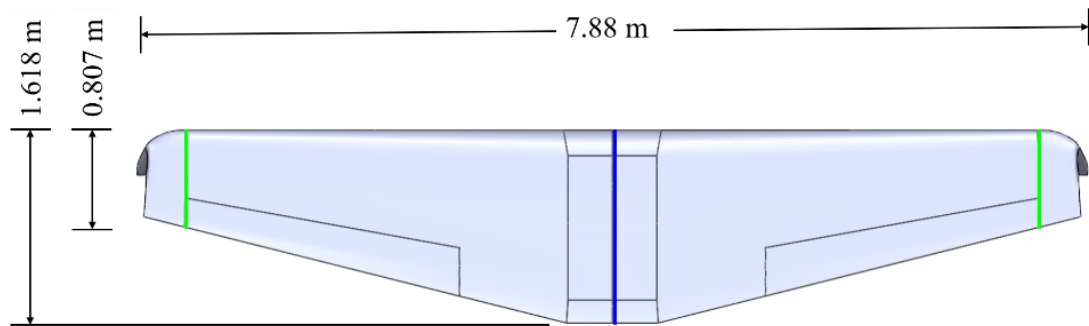


Figure 3.1b: Wing Planform View

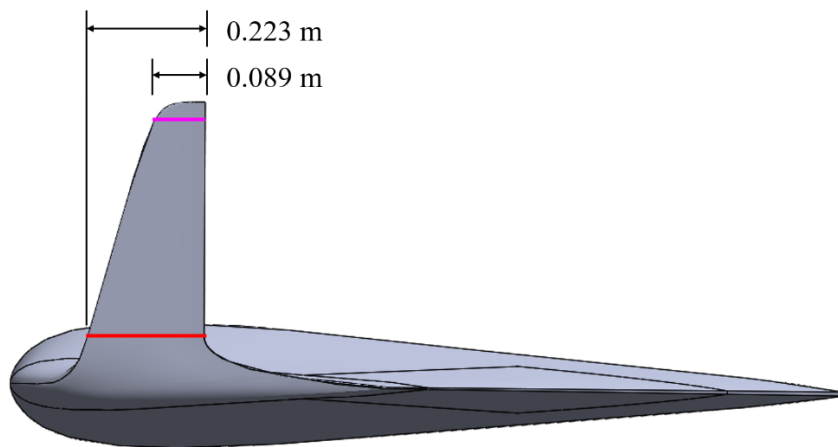


Figure 3.1c: Winglet View

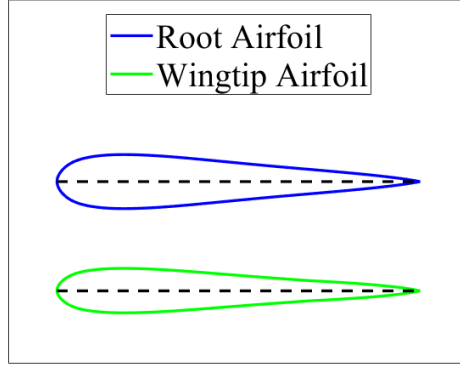


Figure 3.2a: Wing Airfoils

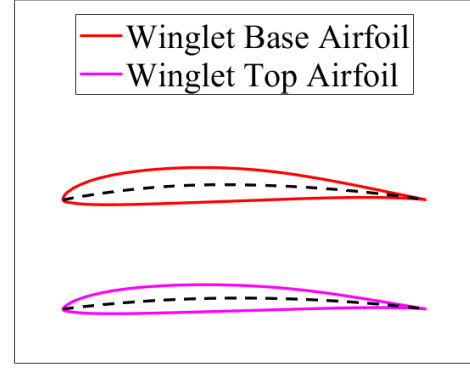


Figure 3.2b: Winglet Airfoils

To analyze this wing using VLM, the wing needs to be discretized into horseshoe vortex strips. Each line in Figure 3.3 represents a line vortex, all of which are connected to form a lattice of vortices. Vortex strips were spaced uniformly across the span of the main wing, as this leads to more accurate results than nonuniform spacing [18]. The vortex strips that constitute the winglets followed a co-sinusoidal spacing, with larger spacing at the bottom of the winglets and closer spacing near the tip of the winglets [19]. Chordwise spacing followed a cosine distribution, with closer spacing of vortex strips near the leading edge and trailing edge of the wing. This type of spacing allows calculations to converge more rapidly and with more accuracy than a uniform spacing scheme [20]. Wing sections were specified at the root, tip, winglet base, and winglet top; the number of vortices and their spacing between these sections were altered to find an appropriate number of panels that produced the most accurate results, as shown later in the VLM convergence study. To allow easy manipulation of the amount of vortex strips that constitute the wing, simplifications were done to the base geometry. The rectangular area at the root of the wing was removed to allow uniform distribution of vortex strips between the wing root and wing tip. The curvature of the wing tip was replaced by straight lines to easily define the number of vortices between the wing tip and the base of the winglet.

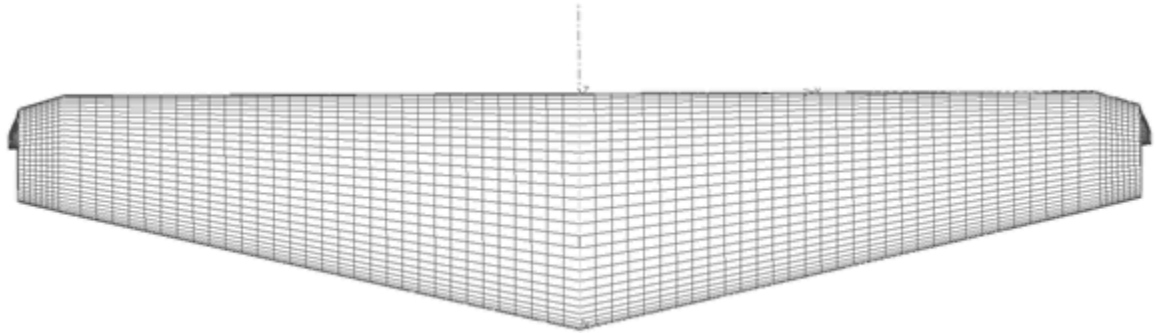


Figure 3.3: Vortex Lattice Model

3.2 Determination of Flight Conditions

For this study, lift and drag characteristics of winglet camber configurations were analyzed for different flight conditions. Winglets tend to be detrimental at lower lift conditions like steady level flight since induced drag is not significant at this flight condition; any decrease in induced drag here due to the winglets' effect on the wingtip vortex does not account for the increase in parasitic drag due to the wetted area of the winglets. This study aims to determine if changing winglet camber can reduce the parasitic or induced drag enough to show a noticeable decrease in total drag.

The two flight conditions tested represent two separate flight regimes that an aerobatic race aircraft is likely to fly: steady level flight at 200 knots and an 8g turn at 200 knots. Table 3.1 below lists the flight conditions used for all VLM tests. The reference area is based on the planform projection of the wing with winglets and was kept constant for all tests. Reference chord is based on the mean aerodynamic chord of the wing and was also kept constant. Standard atmosphere at sea level was assumed for simplicity; 200 knots converts to 102 m/s, which is Mach 0.297 at sea level. The threshold for compressibility effects to become noticeable is Mach 0.3; since this speed is less than this threshold, air density was kept constant at the standard atmosphere value at sea level. The value for mass specified here refers to the aerobatic weight for Red Bull Air Racers and

was needed in order to determine how much lift was necessary to produce steady level flight, and the 8g load factor for the turning condition.

Table 3.1: Flight Conditions for Steady Level Flight and 8g Turn

Steady Level Flight, 200 Knots		8g Turn, 200 Knots	
Airspeed	102 m/s	Airspeed	102 m/s
Mass	700 kg	Mass	700 kg
Target C_L	0.1191	Target C_L	0.9634
Air Density	1.225 kg/m ³	Air Density	1.225 kg/m ³
Reference Area	9.04 m ²	Reference Area	9.04 m ²
Reference Chord	1.213 m	Reference Chord	1.213 m

For each flight condition, a target lift coefficient was used to match all winglet configurations instead of an angle of attack because changing the winglet camber alters the lift produced for a given angle of attack. This means that for a given amount a lift, the angle of attack required to produce this lift will be different based on the winglet camber. To ensure that the comparison for each winglet configuration is based on the lift required for each flight condition, lift was set to be constant and angle of attack was allowed to vary.

3.3 VLM Analysis

VLM is a method that is best suited for aerodynamic configurations that consist of thin lifting surfaces at small angles of attack [17]. This method was used to calculate lift and lift-induced drag based on the vorticity measured in the far-field Trefftz plane. Since the method only uses thin surfaces, it neglects viscous effects due to airfoil thickness. However, it is necessary to include effects of viscosity on the total forces and moments acting on a wing since total drag is the summation of viscous drag and induced drag.

3.3.1 Calculation of Aerodynamic Forces for VLM

In order to calculate viscous properties of a wing, a two-dimensional panel method was used. This panel method calculated aerodynamic characteristics for the airfoil sections that constitute the two-dimensional cross sections of the wing, based on the coupling of inviscid potential flow equations and boundary layer calculations. For this study, the open-source software

XFLR5 was used to conduct batch analysis of airfoil sections that constitute the wing used in this study. XFLR5 is based on the XFOIL program, which is used to conduct two-dimensional panel method analysis. XFLR5 uses a high-order panel method combined with fully coupled viscous/inviscid interaction to obtain aerodynamic properties of airfoils at user-specified conditions. Through the interaction of incompressible potential flow and boundary layer formation equations, parasitic drag for an airfoil can be calculated. These calculations were performed for airfoils that constitute the root and tip of the wing, as well as the base and the top of the winglet [19]. For intermediate wing sections between the wing root and tip, viscous drag is interpolated based on the local wing lift [20].

XFLR5 uses the e^N method to predict boundary layer transition for steady two-dimensional flows, based on linear stability theory [21]. For this method, transition occurs when the local instability amplification rate based on velocity profile exceeds a certain threshold N , which is typically set between 7 and 9 [22]. In addition, XFLR5 allows users to set a forced transition location along the chord of an airfoil. Transition may occur when the Reynolds number based on momentum thickness exceeds the transition criterion as shown below in equations 1 and 2 [23]. For a freestream airspeed of 102 m/s, transition occurs at 0.07 m along the chord, as shown in Figure 3.4. This was set to be forced transition location for all airfoils along the span of the wing, including the winglets as shown in Figure 3.5.

$$\text{Momentum Thickness:} \quad \theta = \frac{0.73x}{\sqrt{Re_x}} \quad 1$$

$$\text{Transition Criterion:} \quad Re_\theta > 1.174 \left(1 + \frac{22,400}{Re_x} \right) Re_x^{0.46} \quad 2$$

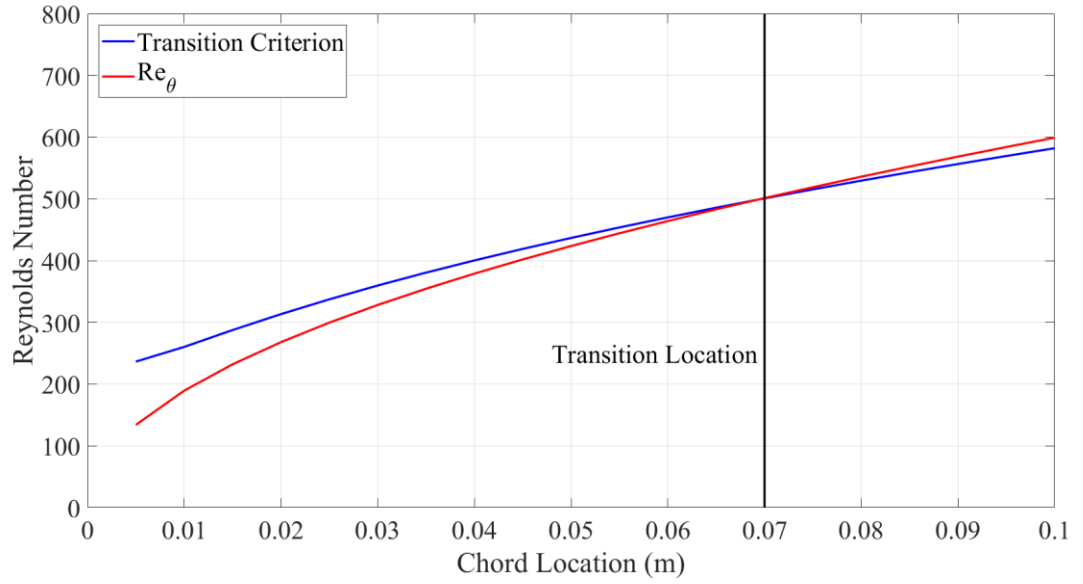


Figure 3.4: Transition Criterion

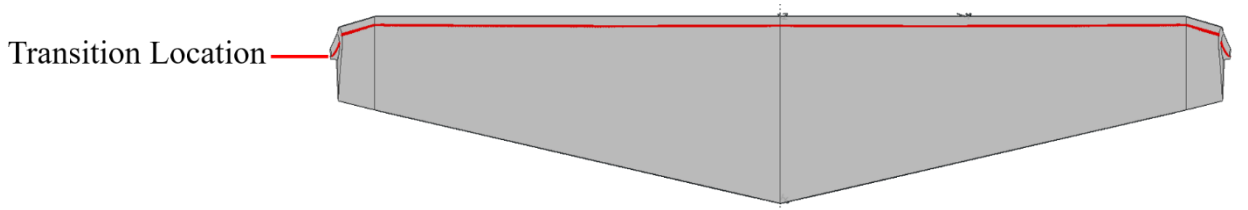


Figure 3.5: Location of Forced Transition on the Wing

Once the parasitic drag has been obtained for a given flight condition, VLM was used to determine the induced drag for that same flight condition. For this study, Athena Vortex Lattice (AVL) was used to conduct VLM analysis of the entire three-dimensional wing. AVL was widely used to conduct similar analysis on lifting bodies. AVL uses thin airfoil theory to determine the lift slope of the two-dimensional wing sections that constitute the wing. These sections are modeled to have the same shape as the camber line of the airfoil for those sections. Thin airfoil theory relates angle of attack to lift for incompressible and inviscid flows; because of these assumptions, thin airfoil theory cannot be used to calculate parasitic drag, which is a measure of viscous forces [24]. Therefore, VLM can only calculate lift and induced drag. Combining the parasitic drag calculated in XFLR5 with the induced drag calculated in AVL produces total drag for a given flight condition.

It should be noted that thin airfoil theory assumes a linear relation of lift to angle of attack since this method calculates lift based on inviscid theory. As such, this method cannot accurately predict stall, which occurs at high angles of attack due to boundary layer separation. This also means that the lift produced around the stall angle cannot be accurately calculated with this method, so the accuracy results from tests at higher angles of attack are dubious.

As mentioned before, VLM uses thin airfoil theory to determine the local lift slope of airfoil sections on a wing. Thin airfoil theory assumes the lift curve slope is 2π ; this is true for all airfoils using this theory. However, increasing the airfoil's camber lowers its zero-lift angle of attack. This means that for a given angle of attack, a cambered airfoil should produce higher lift. VLM determines the effective angle of attack for each spanwise section of the wing and relates this to each section's individual lift curve described by its camber. Based on this, the lift for each section can be calculated [25]. Integrating the sectional lift over the entire wingspan produces total lift for the wing, as shown in equation 3. L represents total lift and L' is the lift due to each wing section based on its spanwise position on the wing, y .

Total Lift Calculation:
$$L = \int_{-b/2}^{b/2} L'(y) dy \quad 3$$

The method by which induced drag is calculated in VLM involves the integration of the Trefftz plane. The Trefftz plane is a plane placed downstream of a wing in a flow field, perpendicular to the freestream. Wingtip vortices induce flow velocities normal to the freestream, which appear as a region of circular flow in the Trefftz plane. Induced drag for inviscid, incompressible flow over a finite-span wing can be obtained from the integration of these velocities as shown in equation 4. Assuming the freestream flow is oriented along the x-axis in standard cartesian coordinates, v and w represent the normal velocities to the freestream along the y and z-axes respectively [25].

Induced Drag Calculation:
$$D_i = \frac{1}{2} \rho_{\infty} \iint_S (v^2 + w^2) dy dz$$
 4

In order to determine how much lift was needed for the high and low g conditions, the base wing with unaltered winglet camber was tested in AVL using the flight parameters from Table 3.1. The result produced an angle of attack that was necessary for the wing to produce enough lift to fly at each condition. The wing was then tested in XFLR5 to obtain the total parasitic drag for this angle of attack. This result for total parasitic drag from XFLR5 was then input into AVL to calculate the total drag for this configuration, based on the combination of the parasitic drag calculated in XFLR5 and the induced drag calculated in AVL. Every winglet camber configuration from this point on used this same method for obtaining parasitic, induced, and total drag, while making sure to match the values for required lift found here with the base wing.

3.3.2 Cambered Winglet Analysis

In order to analyze the effects of winglet configuration, the lift and drag characteristics were determined for a combination of winglet hinge location along the chord of the winglet and flap deflection. The hinge was located on the existing winglet chord to ensure that the size of the winglet did not change and was set to 80%, 50%, and 20% of the winglet chord where the 80% chord hinge is closest to the trailing edge and 20% is closest to the leading edge of the winglet. These values were chosen initially since they represent a wide range of locations across the winglet chord. Winglet flap deflection was originally set to be 0° , $\pm 2^\circ$, $\pm 3^\circ$, and $\pm 5^\circ$ to provide a narrow range of deflections from which trends in efficiency due to flap deflection can be observed. Figure 3.6 shows the convention used for hinge location and flap deflection for the winglet airfoil, where positive deflections increase the camber curvature and negative deflections decrease camber curvature.

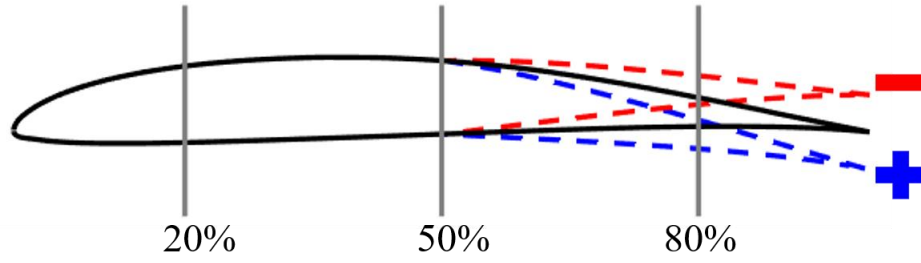


Figure 3.6: Winglet Configuration Convention

Based on initial analysis of the changes in total drag on the wing based on winglet configuration, the actual difference in drag was too small to be compared directly. To better understand the effect of winglet configuration on wing total drag, the winglet configurations were compared in terms of a percentual to the winglet with no flap deflection. Lift and drag was normalized into coefficient of lift (C_L) and coefficient of drag (C_D) and was dependent on the wing angle of attack and winglet configuration. Since parasitic and induced drag were calculated using separate methods, they were compared separate to each other for each winglet configuration. The other main point of comparison between the configuration is the wing efficiency, which is the ratio of the lift the wing produced divided by the drag it produced and is shown below by equation 5. Equation 6 shows the method used for obtaining the percentual in efficiency for each winglet configuration, showing the relative improvement or diminishment of efficiency for each configuration compared to the base winglet performance.

$$\text{Efficiency:} \quad E = \frac{C_L}{C_D} \quad 5$$

$$\text{Efficiency Percentual:} \quad \delta_{Efficiency} = 100 \times \frac{E_{Camber} - E_{No\ Camber}}{E_{No\ Camber}} \quad 6$$

In addition to efficiency analysis for the two flight conditions, the total lift, total drag, induced drag, and parasitic drag forces were analyzed over a wide range of C_L for two different winglet configurations in order to observe the overall effect that these winglet configurations have compared to a winglet with no flap deflection. Based on the results for the efficiency analysis at

the two flight conditions, the 50% hinge location at $+5^\circ$ and -5° deflection winglet configurations were chosen because of their noticeable effect on wing efficiency and ease of convergence in VLM and the two-dimensional panel method.

3.3.3 Panel Method Convergence Study

Before testing winglet camber configurations, convergence studies were conducted for the two-dimensional panel method to find the least amount of panels necessary to model the wing's airfoils, without adversely affecting results based on numerical discretization of the airfoil. The panel method convergence study was carried out in XFLR5, using the airfoil from the root of the wing. This study was conducted at 102 m/s, which corresponds to 200 knots, the speed at which all future tests for this wing were conducted. Since the airfoil was symmetric, the angle of attack was set to 5° to provide a non-zero value for lift from which changes to lift coefficient may be observed based on total number of panels. In addition to lift, drag was also observed based on total numbers of panels. These panels were refined closer to the leading and trailing edge to better resolve the curvature and pressure distribution over these areas, as shown in Figure 3.7. The trailing edge was extended to produce a sharp point to satisfy the Kutta condition for the panel method [26].

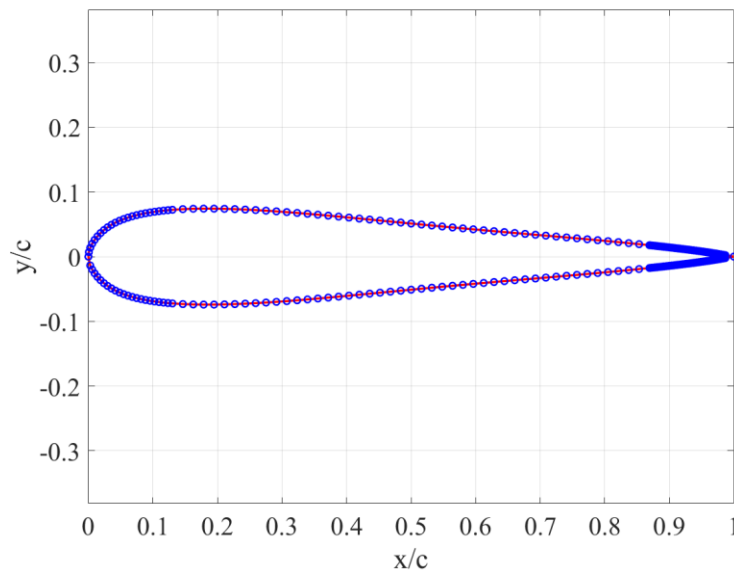


Figure 3.7: Distribution of Airfoil Panels

For convergence studies, the equations 7 and 8 were used for calculating the percentual for lift and drag based on increasing levels of refinement. Since there is no base set of data from which to calculate deviation for this airfoil, the percent difference for each refinement level was calculated based on their deviation from the previous total panel amount: $C_{l\text{ current}}$ and $C_{d\text{ current}}$ refers to the lift and drag for the current level of refinement being analyzed and $C_{l\text{ previous}}$ and $C_{d\text{ previous}}$ refer to the lift and drag from the previous level of refinement. The condition for convergence was a total panel amount that produced minimal change compared to its preceding panel amount.

$$\text{Lift Coefficient Percentual:} \quad \delta_{C_l} = \left| 100 \times \frac{C_{l\text{ current}} - C_{l\text{ previous}}}{C_{l\text{ previous}}} \right| \quad 7$$

$$\text{Drag Coefficient Percentual:} \quad \delta_{C_d} = \left| 100 \times \frac{C_{d\text{ current}} - C_{d\text{ previous}}}{C_{d\text{ previous}}} \right| \quad 8$$

Figure 3.8 shows the results for airfoil C_l versus number of panels, where the refinement level showed the same variation in C_l and C_d past 125 panels. This means that using any more than 125 panels for the airfoil will not significantly reduce the difference in the aerodynamic forces calculated by this method due to panel resolution. As such, 125 panels may be used for this study.

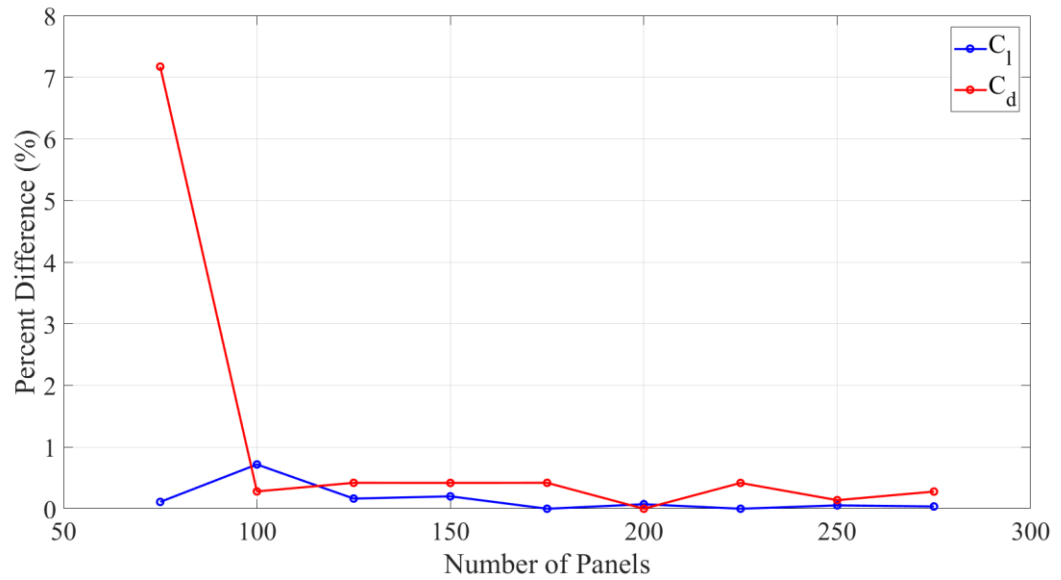


Figure 3.8: Panel Method Convergence Study

3.3.4 Vortex Lattice Method Convergence Study

Since VLM models a wing with horseshoe vortex strips in three-dimensional space, a different discretization method than what was used in the two-dimensional panel method needed to be used. For the main wing used in this study, only the wing root and tip locations, size, and airfoil shape were defined. Between these sections, AVL interpolated intermediate wing sections and their airfoil camber. The user determines the total number of interpolated sections and their distribution scheme between each defined wing section, as well as the total number of chordwise vortex strips and their distribution.

The spanwise distribution for this study was conducted first and used the same speed and angle of attack as the panel method. Spanwise sections were defined for a half-span of the wing, such that the total number of sections that were used to model the wing were double the amount listed here since the wing needed to be mirrored at the root to produce a full span. To ensure consistency with the results, the number of chordwise vortices was set to 50, which was the maximum number of chordwise points allowed by AVL. Like the panel method convergence study, relative changes in lift and drag for the entire wing was compared between the total number of wing sections, where the least amount of change between 2 sequential settings determined convergence.

Figure 3.9 shows that the relative change in lift between any 2 refinement levels was below 0.1%, with error being as small as 0.002% at 52 wing sections. AVL has a maximum limit of 6000 vortices to model any given geometry, and at 52 wing sections most of these vortices are being used to model just the wing.^[12] As such, fewer than 52 sections needed to be used in order to have enough vortices to model the winglets later on. Compared to lift, wing drag exhibited larger error with increasing number of wing sections. The reason there was more change as the number of wing sections increased was because these sections are modeled as vortices with a singularity at the centerline defined by the exact locations of these sections. As the number of wing sections increased, these sections were spaced closer together, leading to more interaction between neighboring vortex singularities. This interaction caused variations in the resulting wingtip vortex, from which induced

drag was calculated, leading to variations in drag. As such, it was necessary to avoid a total number of wing sections that produce too small of a spacing between sections, so 32 wing sections were chosen as a compromise between obtaining accurate lift calculations and avoiding small spacings that can affect drag calculations.

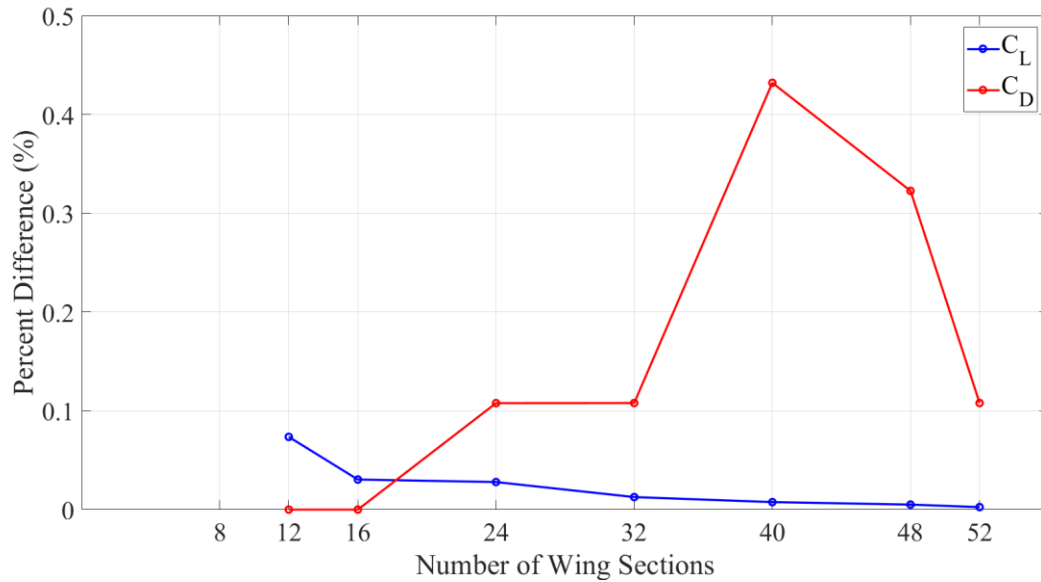


Figure 3.9: VLM Spanwise Wing Convergence

After the conclusion of the spanwise convergence study, a chordwise convergence study was conducted to minimize the total number of vortices used in these calculations. For this convergence study, the number of spanwise sections was kept at 32 while the total number of chordwise points for each section was varied. As shown in Figure 3.10, there was little variation in lift with number of chordwise vortices with most refinement levels producing less than 1% difference from each other. It should be noted that 30 vortices produced the least amount of change for this study with an error of less than 0.01%. Since 30 points produced the smallest change in lift as well, this was used as the total number of chordwise points for all VLM models for the main wing.

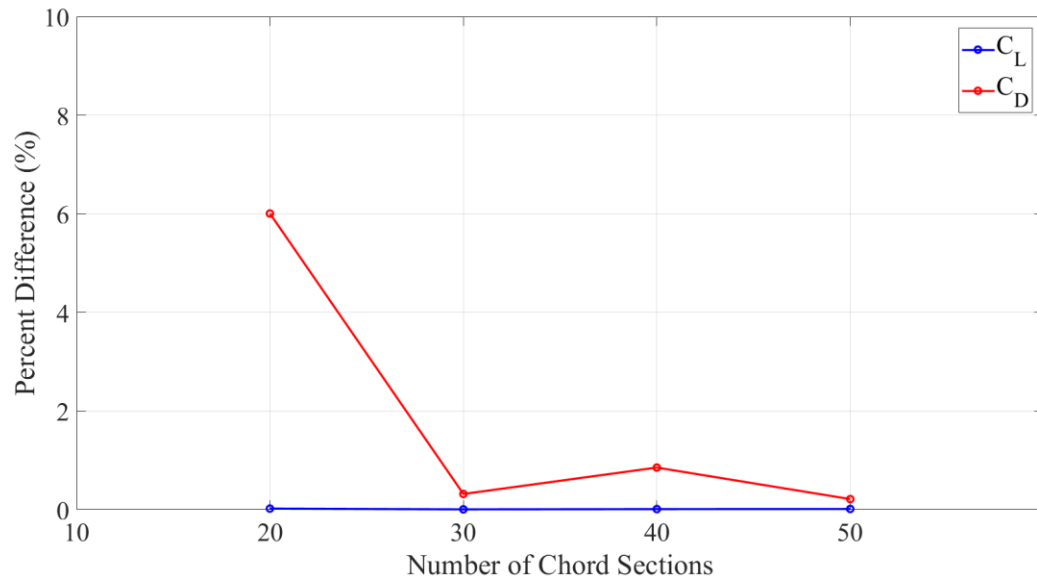


Figure 3.10: VLM Chordwise Wing Convergence

A separate spanwise convergence study was conducted for the winglets, using the same speed and angle of attack that was used in the main wing test. The base wing modeled for this convergence test had 30 chordwise points and 32 spanwise sections, and in order to keep consistency with the main wing, 30 chordwise points were used for the winglets. Compared to the main wing, the winglets produced error of similar magnitudes for both lift and drag, as shown below in Figure 3.11. 16 sections for the winglet produced the least amount of error for drag at 0.2%, but the number of winglet sections can be reduced to as little as 8 sections and still not result in error above 0.4%. Although 16 sections would be ideal based on this study, the limiting factor for number of winglet sections was tied to the how XFLR5 calculated parasitic drag for interpolated airfoils. XFLR5 has a three-dimensional VLM suite to interpolate parasitic drag for the intermediate sections between the base and top of the winglet, but has difficulty interpolating viscous drag data if the wing sections are too close together, specifically at higher angles of attack where the two-dimensional panel method ceases to converge. The interpolated airfoils on the winglet may produce lift conditions outside of the converged flight envelope for the defined airfoil sections, but it was found that reducing the total number of wing sections can get rid of these

problematic sections. As long as the final number of winglet sections was between 8 and 16, the error due to winglet discretization should remain below 0.4%. For this wing setup, 10 winglet sections were the maximum number that allowed for convergence at all angles of attack tested.

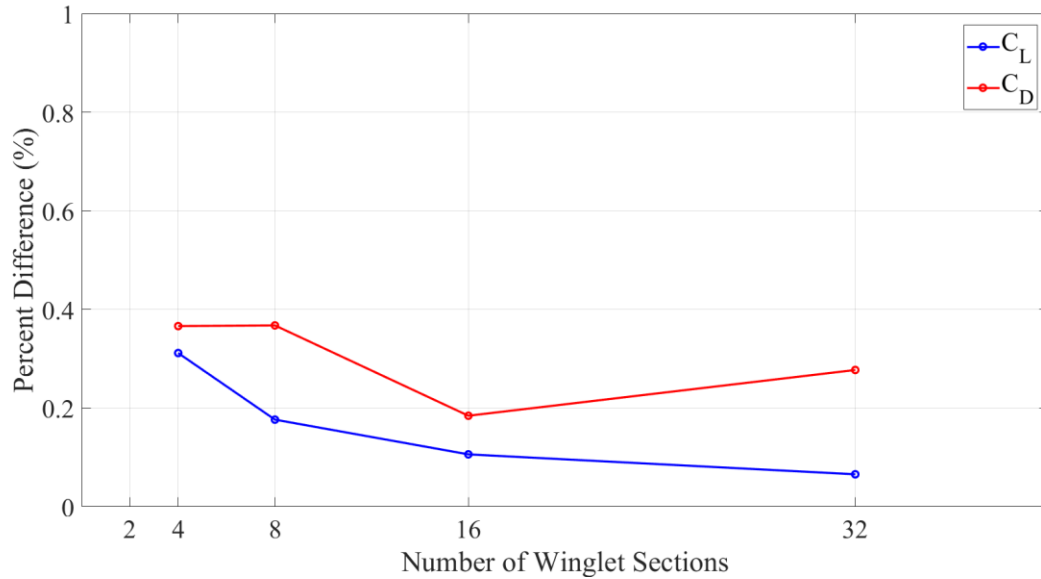


Figure 3.11: VLM Spanwise Winglet Convergence

In summary, 200 panels were used to model all airfoils for two-dimensional aerodynamic analysis in XFLR5. The VLM model consisted of 32 wing sections and 10 winglet sections, with each section having 30 chordwise points.

3.4 RANS Analysis

In order to determine the validity of the AVL and XFLR5 results, aerodynamic forces were calculated using steady RANS. RANS is a numerical computation method used for calculating aerodynamic forces like lift and drag of a geometry moving through a fluid, but instead of modeling the geometry with vortex sheets or panels like VLM, RANS aims to solve the Navier-Stokes equations through fluid domain discretization and three-dimensional flow modelling. Instead of using a Trefftz plane and potential flow equations with viscous integration to solve for induced drag and parasitic drag separately, RANS calculates total lift and total drag through the integration of shear and pressure forces acting on the surface of an object in a flow field. The program used

for these simulations was Simcenter STAR CCM+, a computational fluid dynamics software owned by Siemens Industry Software Inc.

3.4.1 Description of RANS Geometry

Models in RANS simulations are simplified in order to resolve the airflow around a wing in a reasonable amount of time. The model used in these RANS simulations maintains the simplified trapezoidal wingspan as seen in the VLM results to maintain consistency between major model components. However, the wingtips in the RANS model must include smooth transitions between wing sections since sharp chord breaks may have adverse effects on the flow field. Therefore, this geometry should mimic what the wing would look like in reality, and thus produce similar results to the actual wing. For these simulations, all parts of the wing were modeled as no-slip walls, which allowed a boundary layer to form on the surface of the wing and enabled calculation of shear stresses tangential to the wing surface.

Figure 3.12 shows the fluid domain that was modeled around the wing geometry. Since the wing is symmetric, only half of the wing and fluid domain was modelled with a symmetry plane placed at the root of the wing. This reduces the number of cells needed to model the domain by one half, greatly reducing the computational cost of these simulations. A velocity inlet was initially placed 100 chord lengths to the front of the wing geometry, with a constant 102 m/s freestream towards the wing. A half-hemisphere was used to model the inlet to reduce mesh size. Since the velocity vector was set to a specified direction, the curvature of the inlet did not affect flow direction. All other domain boundaries were initially placed 100 chord lengths away from the wing and were set to be pressure outlets, allowing mass flow out of and backflow into the domain. Backflow coming from turbulent structures is extrapolated based on the flow direction of the interior of the domain, which allows mass to leave the domain from all directions, except for the inlet boundary.

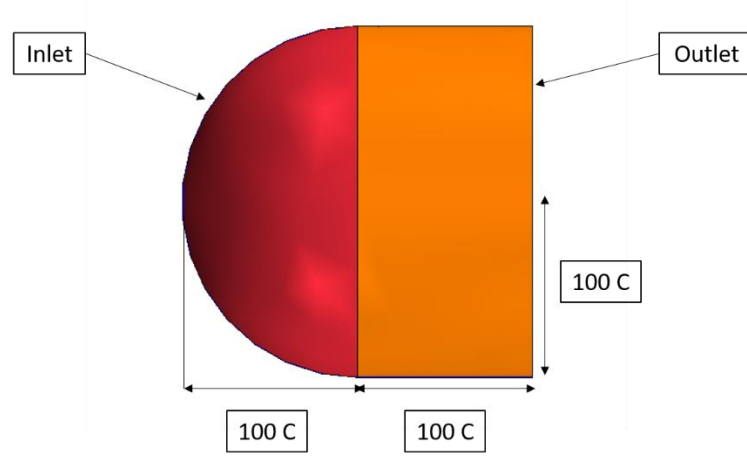


Figure 3.12: RANS Domain, $c = 1.6m$ Root Chord Length

3.4.2 Calculation of Aerodynamic Forces for RANS

Equation 9 shows how aerodynamic forces in RANS are calculated based on the pressure and shear stresses acting on a body in the flow field [27]. f refers to a surface immersed in a flow field and n_f is a user-specified direction vector. If n_f is specified along the axis of freestream flow, then total drag will be calculated. Likewise, if n_f is specified perpendicular to the freestream, lift will be calculated.

RANS Force Calculation:
$$F = \sum_f (F_f^{pressure} + F_f^{shear}) \cdot n_f \quad 9$$

In order to compare the accuracy of VLM induced drag calculations, induced drag needed to be calculated in RANS as well. The method for obtaining induced drag in RANS simulations is by integrating the velocity field in a plane behind this object using equation 4, similar to how Trefftz plane integration is used to obtain induced drag in VLM. The Trefftz plane in VLM is set to capture the far-field flow effects for inviscid flow, but RANS simulations implement turbulence models that present viscous forces into the flow field, which has the effect of dissipating the wake after a certain distance. As shown in Figure 3.13, calculated induced drag approaches a converged value when the Trefftz plane is placed 5 meters behind the wing, while any placement closer to the wing would produce higher estimations for induced drag. Parasitic drag was obtained by subtracting the

induced drag calculated by wake integration from the total drag calculated by surface pressure and shear stresses.

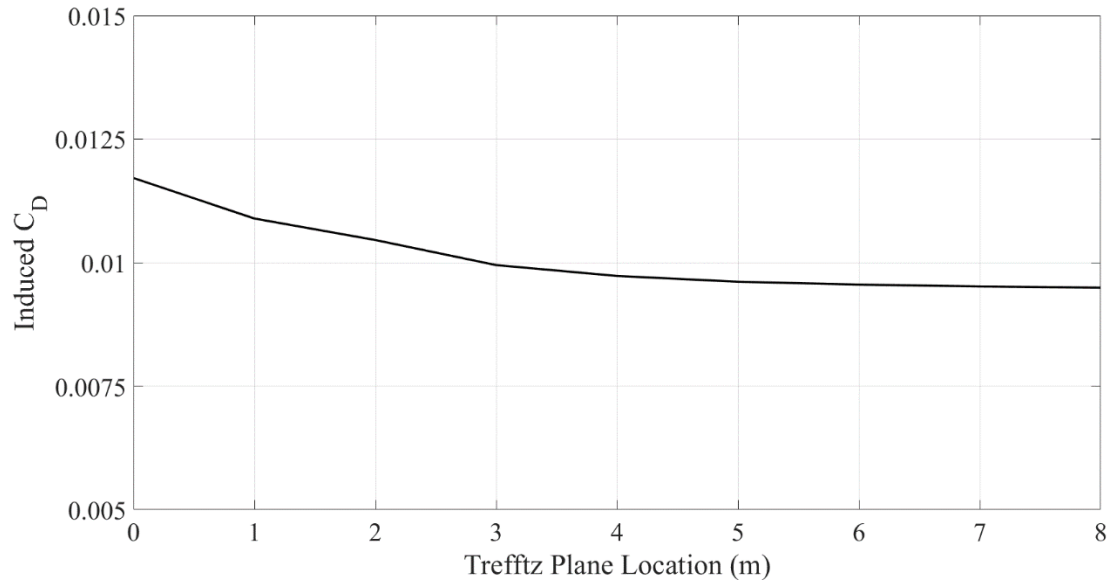


Figure 3.13: RANS Induced Drag Versus Trefftz Plane Location

3.4.3 RANS Flow Characteristics

Table 3.2 shows the continuum and reference values used in the simulation, which reflect the flow conditions used in the VLM simulations to maintain consistency between these two methods. The Realizable k- ϵ turbulence model was used for its robustness and ease of convergence compared to other turbulence models

Table 3.2: Continuum and Reference Settings

Field:	Value:
Freestream Velocity	102 m/s
Air Density	1.225 kg/m ³
Air Kinematic Viscosity	1.855e-5 Pa-s
Turbulence Model	Realizable k- ϵ
Reference Area	4.52 m ²
Reference Chord	1.61 m
Angle of Attack	0°

3.4.4 RANS Mesh Convergence Study

RANS simulations operate by discretizing a fluid domain into finite-volume cells, from which fluid properties like velocity and pressure are calculated. Sufficiently modelling a geometry in a fluid flow may require millions of cells from which millions of calculations are made, requiring significantly more processing power than VLM or other lower-fidelity methods. In order to minimize the processing power required to simulate the flow and therefore reduce run times, a mesh refinement study must be conducted to determine the smallest mesh size that produces the most accurate results. A grid-independence study was conducted in parallel to the domain size study to determine the effect of core mesh cell size on the convergence of the simulations, and additional levels of refinement were added later for cases where a simulation initially diverged with the base settings.

Table 3.3 lists the mesh settings held constant throughout the domain study. Base size of the cells was initially set to 5 meters and was used to model the far field domain cells that would not be experiencing any flow effects from the wing. On the wing and winglet, the target size was set to 0.1% of the base size and the surface curvature was set to 720 points per circle: to allow accurate modelling of the curvature of the wing while maintaining consistent cell aspect ratio. The domain target size was set to 1,000% of base in order to enforce larger cells at the domain boundaries and reduce the total number of cells in the domain; since these areas are so far away from the wing, they should be seeing minimal effects and thus do not need a fine mesh to resolve the flow.

Table 3.3: Mesh Settings

Field:	Value:
Base Size	5 m
Surface Curvature	720 points/circle
Prism Layer Total Thickness	0.03 m
First-cell Height	4.103e-6 m
Total Number of Prism Layers	20
Wing Target Size	0.1%
Winglet Target Size	0.1%

Figure 3.14 shows the aspect ratio of the base mesh near the wing. The reason the wing surface has low aspect ratio is because the prism layer first cell height is $4.0\text{e-}6$ meters, compared to its width of $5.0\text{e-}3$ meters. This is acceptable because the wall velocity for viscous flow is 0 m/s , which means that there is no flow movement that needs to be resolved on the wing surface. There is very little change in the boundary layer velocity profile along the chord or span of an object, which means that cells in the boundary layer can be much wider and longer than they are tall. However, the boundary layer velocity profile changes significantly normal to a surface in the flow field and requires the nondimensional wall y^+ as described by equation 10 to be between 1 and 3 to capture this gradient accurately, using the $k\text{-}\epsilon$ turbulence model. For the flow velocity and kinematic viscosity used in these simulations, a first-cell height of $4.0\text{e-}6$ produces a wall y^+ of 1. The total boundary layer height for the longest chord length in these flow conditions was calculated using equation 11 and found to be 0.024 meters, so the total prism layer height was set to be $3.0\text{e-}3$ meters in order to resolve a smooth transition between the boundary layer and freestream. 20 prism layers were used to resolve the boundary layer velocity profile with the distribution being automatically determined by STAR CCM+ based on the first-cell height and the prism layer total thickness.

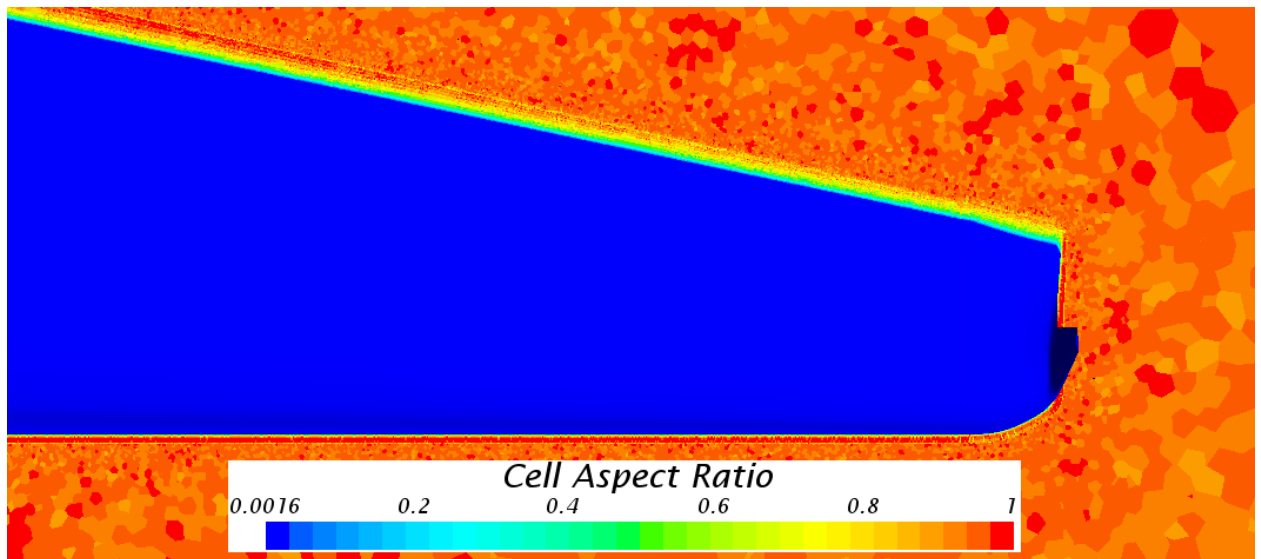


Figure 3.14: Near-wing Cell Aspect Ratio

$$\text{Wall } y^+: \quad y^+ = \frac{u_* y}{\nu} \quad 10$$

$$\text{Boundary Layer Height:} \quad \sigma = 0.37x/Re_x^{1/5} \quad 11$$

Initially, the domain was arbitrarily extended 100 chord lengths away from the wing in all directions to minimize the influence of the flow from the wing on the boundaries of the domain. Based on the fluid velocity in the domain as seen in Figure 3.15, there were no flow effects near any of the boundaries in the domain. From here, the domain was decreased 75 chords, 50 chords, and 25 chords lengths in all directions in an attempt to decrease the total number of cells used in the simulation. In addition, the base size was varied between 10 meters, 7.5 meters, 5 meters, and 2.5 meters to determine the effect of finer and coarser base sizes on grid convergence.

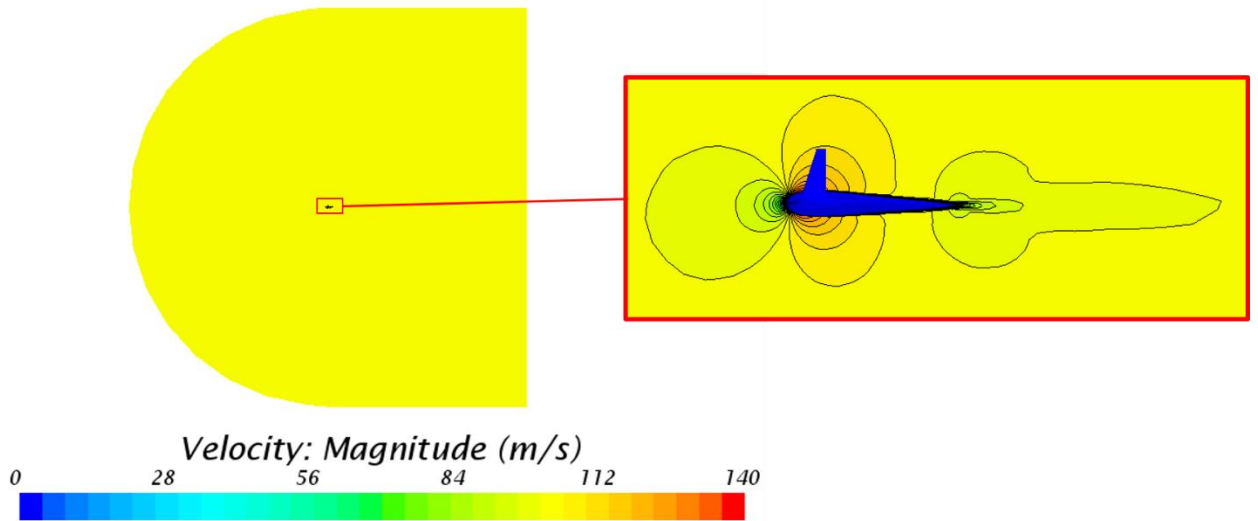


Figure 3.15: Flow Velocity for Base Domain Size

Based upon initial simulations, the turbulence dissipation rate for the 10-meter base sizes did not converge, causing the rest of the simulation to diverge. This could be due to having too low of an aspect ratio for the surface cells on the wing: although it is generally fine to have lower aspect ratio cells on the surface since there is little variation across the surface in the boundary layer, the trailing edges may be too skewed to properly resolve the boundary layer and turbulence dissipation rates at these cells.

The 2.5-meter meshes contained 28 million cells, which required more internal memory than what was available for the computer that was used to analyze these simulations. In order to obtain a finer mesh without exceeding computer memory limits, a base size of 3 meters was used in place of 2.5 meters for the different domain sizes. However, like with the 10-meter base size meshes, the turbulent dissipation rate for all of the 3-meter base size meshes diverged as well. It is uncertain why a finer mesh would diverge while a coarser mesh like the 7.5-meter and 5-meter base size meshes would converge, but this pattern was seen for all the domain sizes tested. As such, only the 7.5-meter and 5-meter base sizes were analyzed for this mesh refinement study.

Table 3.4 shows the cell count for the different domain sizes and base sizes. These values are important since they are proportional to how much memory each simulation requires, as well as the run times required to reach convergence. For a given base size, the total cell count is consistent among all domain sizes and seems to increase with decreasing domain size, which is the opposite of what is expected since smaller domains usually mean fewer cells are needed to fill in the mesh. One reason this may happen is because the automated mesh function inserted more cells between the wake refinement and the domain boundaries in order to satisfy the domain wall boundary conditions. It should be noted that the 100-chord domain size did not include wake refinement, but the total cell count should be proportional to the other domain sizes since the wake area is consistent between all domain sizes. In addition, the 5-meter base size for the 25-chord domain did not converge, so the 25-chord domain cannot be used for this study.

Table 3.4: Total Cell Count

	100 Chords	75 Chords	50 Chords	25 Chords
7.5 m Base Size	3.77 million	3.88 million	4.01 million	3.99 million
5 m Base Size	7.19 million	7.96 million	7.78 million	7.79 million

Since the cell count is consistent between the domain sizes, only the base sizes for 100 chords and 50 chords cases were analyzed for convergence. All simulations converged within 400 iterations, but the 50-chord domain size had higher residuals on average than the 100-chord domain

size. While residuals by themselves are not a valid indicator of convergence, they are important for determining the accuracy of the results, where lower residuals equate to more accurate results since there is less change in the solution of the governing system of equations per iteration. Figures 3.16 and 3.17 depict the residuals for the 5-meter 100-chord domain and the 5-meter 50-chord domain. The continuity residual refers to the conservation of mass equation within the fluid domain while momentum residuals refer to the conservation of momentum equations for three-dimensional flow [28]. Tke and Tdr are the turbulence kinetic energy and dissipation rate respectively and are specific to the equations used to model turbulent flow in the k- ϵ turbulence model. Not only are the residuals lower in the 100-chord domain, but they also have lower fluctuations compared to the 50-chord domain. Fluctuations in the residuals are usually caused by interactions with the domain boundaries, so it follows that the residuals would fluctuate less with the larger domain.

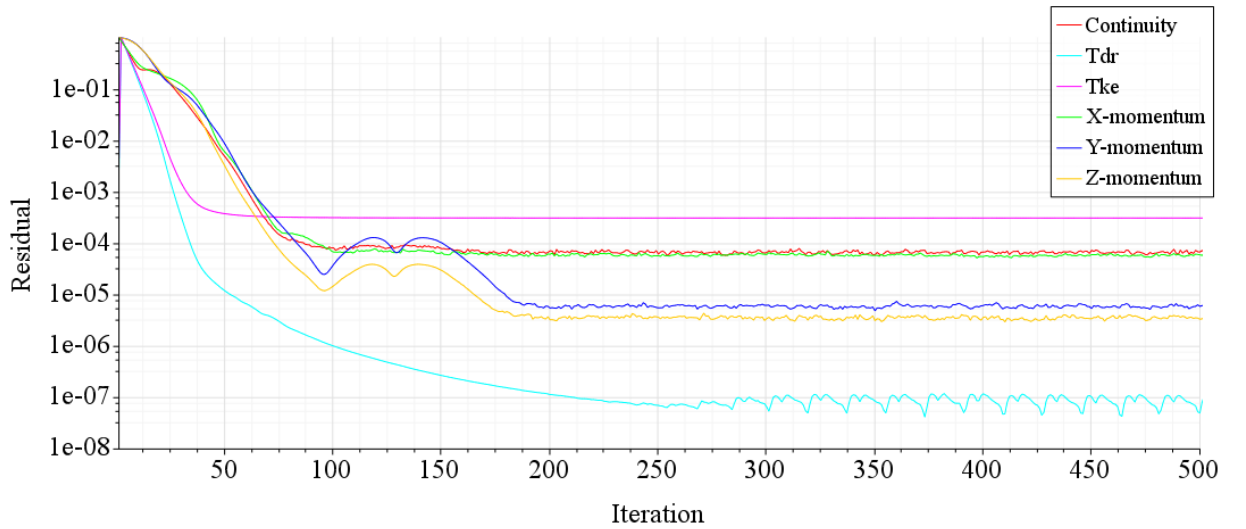


Figure 3.16: 5 m Base Size, 100-Chord Length Domain Residuals

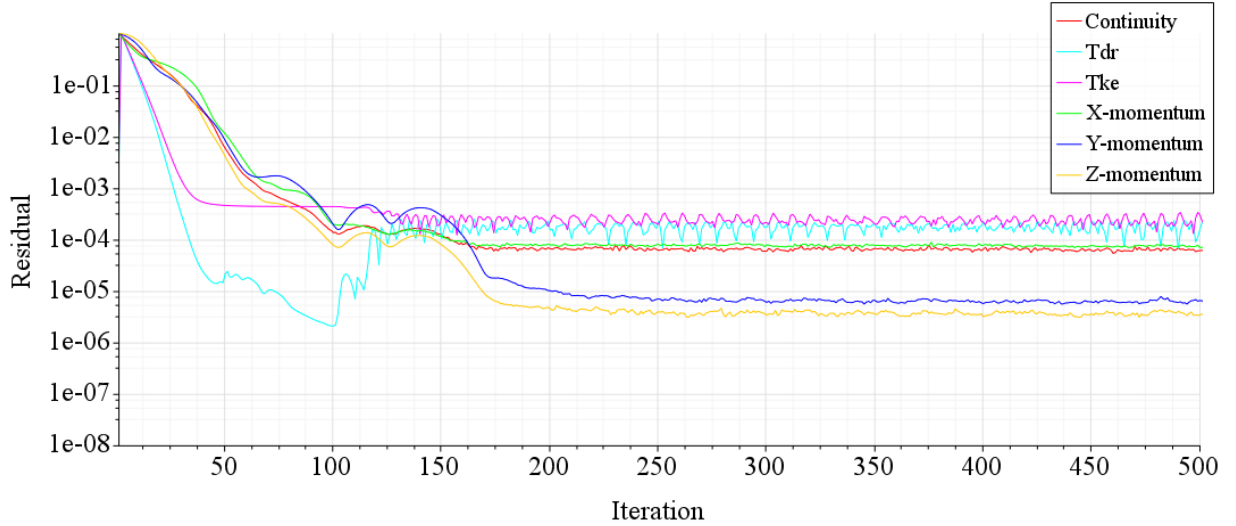


Figure 3.17: 5 m Base Size, 50-Chord Length Domain Residuals

There is a 2.36% difference between the highest and smallest values for lift and 3.07% difference between highest and lowest values for drag as seen in Tables 3.5a and 3.5b. This difference is caused by the lack of wake refinement for the 100-chord size domain. However, even without the wake refinement, there was less uncertainty in the residuals for the 100-chord domain, which means that adding the wake refinement to these meshes should produce results with lower residuals. As such, the 100-chord domain size with 7.5 m base size was used for all RANS simulations for this study, with additional refinement added when necessary to assist in simulation convergence, specifically around the leading edge to better resolve the wing curvature and in the wake region to better model turbulence dissipation.

Table 3.5a: Domain Size Lift Comparison

	100 Chords	50 Chords
7.5 m Base Size	6.68e-2	6.68e-2
5 m Base Size	6.77e-2	6.61e-2

Table 3.5b: Domain Size Drag Comparison

	100 Chords	50 Chords
7.5 m Base Size	9.76e-3	9.76e-3
5 m Base Size	9.47e-3	9.46e-3

3.5 Comparison of Methods

The purpose for using RANS is to validate VLM calculations is to determine where the results from VLM cease to produce realistic answers for aerodynamic forces. VLM is a linear

method, which means that it is only useful for small angles of attack that stay within the linear part of a wing's lift curve. This means that VLM will assume a wing's lift slope is still linear at high angles of attack where in reality the wing would have a nonlinear lift curve. Based on Theory of Wing Sections, symmetric airfoils tend to have nonlinear lift curves at around 10° angle of attack, with stall occurring around 15° [24]. As will be discussed in the results chapter, the wing in the high-g condition produced an angle of attack 11° , meaning that it is possible that the lift curve for this wing may be nonlinear at this condition. Since VLM cannot accurately predict aerodynamic forces in the nonlinear portion of a wing's lift slope, it was necessary to validate whether the lift slope calculated in VLM truly is linear by using the higher-fidelity RANS method.

4.1 RANS Validation of VLM Results

Since VLM requires two different methods to obtain induced and parasitic drag separately, it became necessary to compare these values to the total drag obtained from RANS to ensure that these two separate methods were valid. In order to compare these methods separately, the total drag in RANS was separated into induced and parasitic drag. A range of angles of attack from 0° to 10° was tested to obtain an overall view of the behavior.

4.1.1 Lift Validation

As shown in Figure 4.1, there is no discernable difference between lift calculated in VLM for all tested angles of attack. These angles of attack lie on the linear portion of the wing's lift curve, which is why the results from VLM and RANS match. This is important because the wing needed an angle of attack of 0.65° to produce enough lift to fly at the low g flight condition, while the high g flight condition required 11° angle of attack.

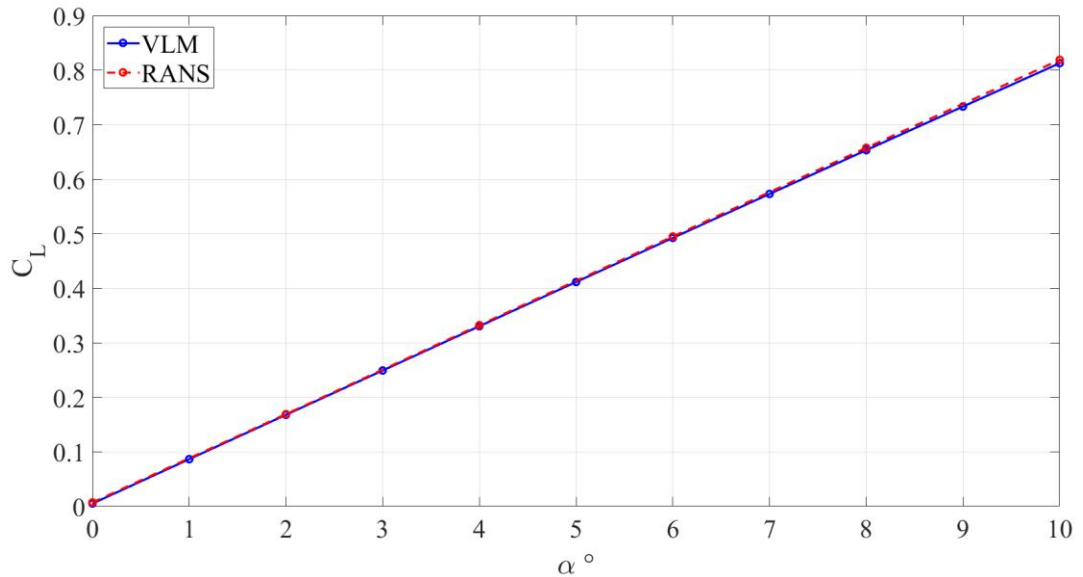


Figure 4.1: VLM Versus RANS Lift Comparison

4.1.2 Drag Validation

VLM requires separate calculation for induced and parasitic drag, whereas RANS calculated total drag as a combination of pressure and viscous forces on the wing. To determine the accuracy of induced and parasitic drag from VLM separately, the total drag calculated from RANS was divided into induced and parasitic drag then directly compared to VLM results.

4.1.2.1 Induced Drag Validation

In Figure 4.2, the induced drag in VLM and RANS follow a parabolic trend. However, VLM overpredicts induced drag above an angle of attack of 4° . This may be due to the effect of Trefftz plane placement in RANS, as the calculated induced drag decreases as Trefftz plane distance from the wing increases.

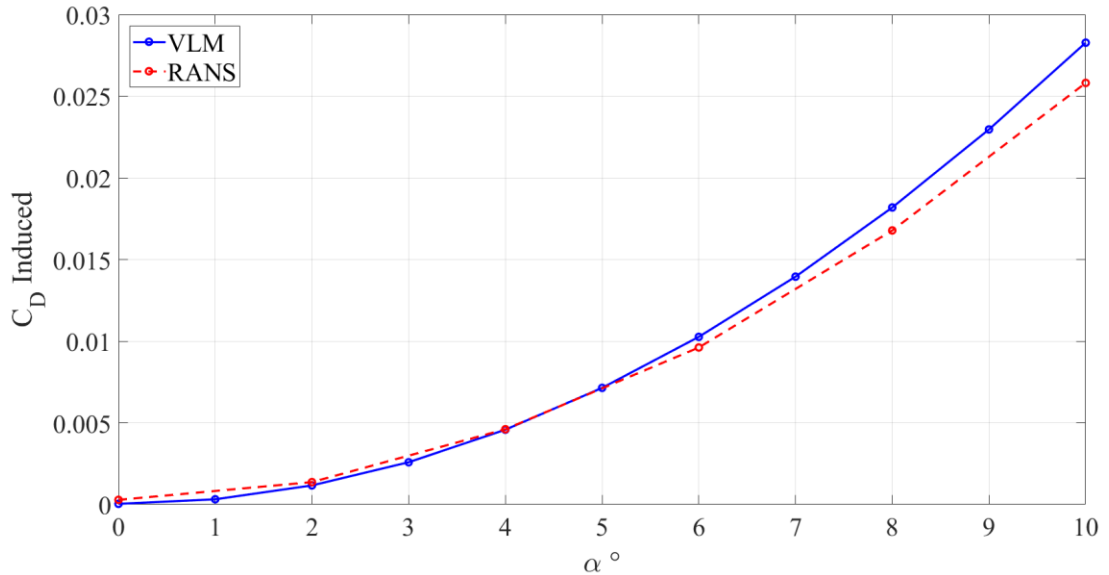


Figure 4.2: VLM Versus RANS Induced Drag Comparison

4.1.2.2 Parasitic Drag Validation

As shown in Figure 4.3, VLM underpredicts parasitic drag for all angles of attack, and this difference in drag increases as angle of attack increases. This may be due to the way turbulence is modeled in VLM and RANS. For this study, VLM used the e^N method for calculating boundary layer transition while RANS used the k- ϵ turbulence model for a fully turbulent flow field. The e^N

method is a lower order method suitable for simple two-dimensional flows but cannot be adapted to more complex three-dimensional flows [21], whereas the k- ϵ turbulence model is more suited for complex three-dimensional flows, so long as there are no strong pressure gradients [29]. The inability for the e^N transition model to calculate complex flow limits its accuracy for determining viscous forces due to turbulence, hence its underpredicting of parasitic drag compared to RANS.

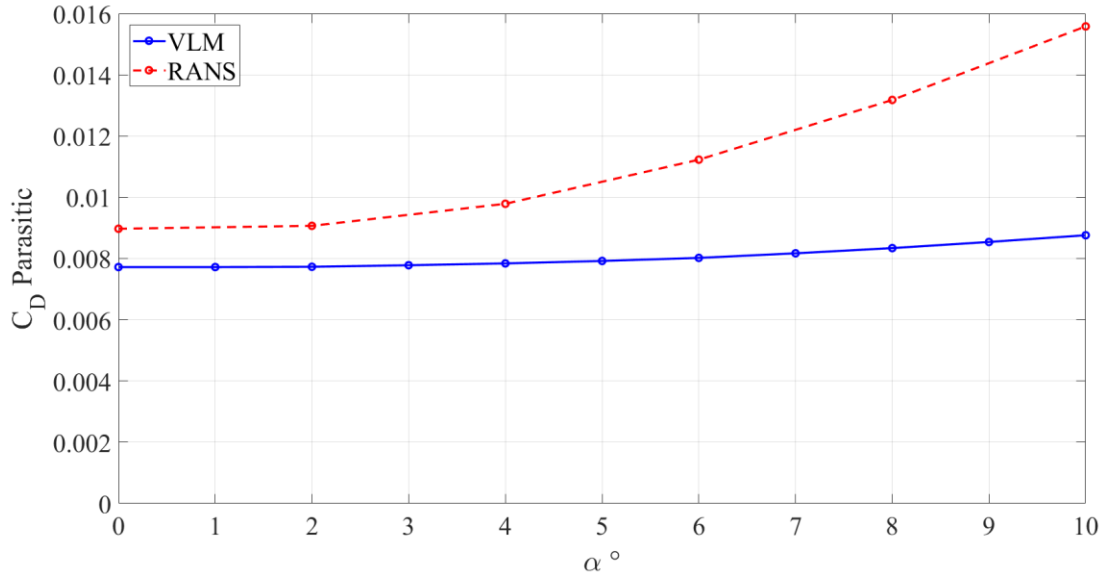


Figure 4.3: VLM Versus RANS Parasitic Drag Comparison

4.1.2.3 Total Drag Validation

As shown in Figure 4.4, VLM underpredicts the total drag compared to RANS for all angles of attack. Even though VLM overpredicts induced drag for higher angles of attack, the effect of underpredicting parasitic drag decreases the value of total drag for these angles. However, the trend between VLM and RANS is the same, following a parabolic increase in drag with increasing angle of attack. These tendencies are adequate for making design decisions for winglets based solely on VLM results, however the absolute values being predicted may be dubious since they do not match with the results from RANS. In order to obtain an accurate value for drag, a more robust and higher-fidelity method like RANS or experimental wind tunnel or flight testing should be used.

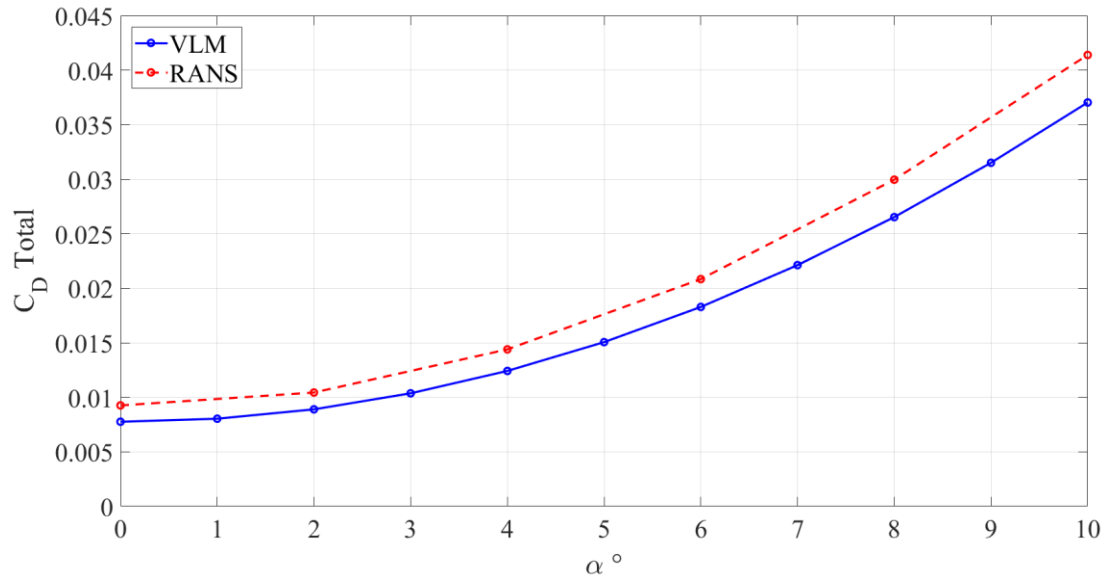


Figure 4.4: VLM Versus RANS Total Drag Comparison

4.2 Winglet Camber Analysis

With VLM validated against RANS, the next step of this study was to analyze the effect of cambered winglets on the aerodynamic forces produced by this wing. VLM allows for easy manipulation of flap hinge location and deflection, so it was used to obtain these forces. To better understand the overall effect of winglet camber changes on the aerodynamic forces produced by the entire wing, the behavior for winglets with a hinge at 50% chord and deflected $+5^\circ$ and -5° was compared to a winglet with no flap deflection for a range of angles of attack and C_L . The low g steady level flight at 200 knots C_L of 0.1191 and the high 8g turn at 200 knots C_L of 0.9634 are denoted in the following figures.

4.2.1 Camber Effects on Airfoil Drag

Figures 4.5 and 4.6 show the change in airfoil parasitic drag versus angle of attack for the airfoil at the base of the winglet and the top of the winglet, respectively, with the effective angle of attack for each airfoil at the low g condition being denoted as circles on the respective lines. Changing the flap deflection has the effect of shifting the drag polar for these airfoils. It is possible for -5° to produce less parasitic drag than the other configurations for both the top and bottom

winglet airfoils if the effective angle of attack of these airfoils is greater than 0° . However, the effective angle of attack for these airfoils at the low g condition is around -2° , where a negative flap deflection increases the parasitic drag compared to no flap deflection. Conversely, a positive flap deflection results in less parasitic drag for this condition.

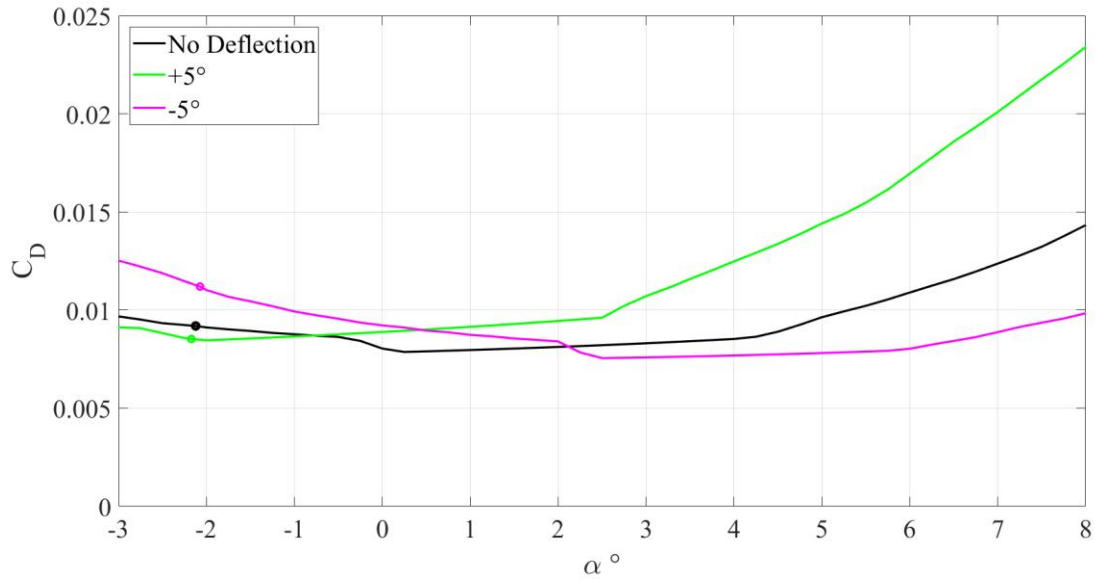


Figure 4.5: Winglet Base Airfoil Parasitic Drag Polar

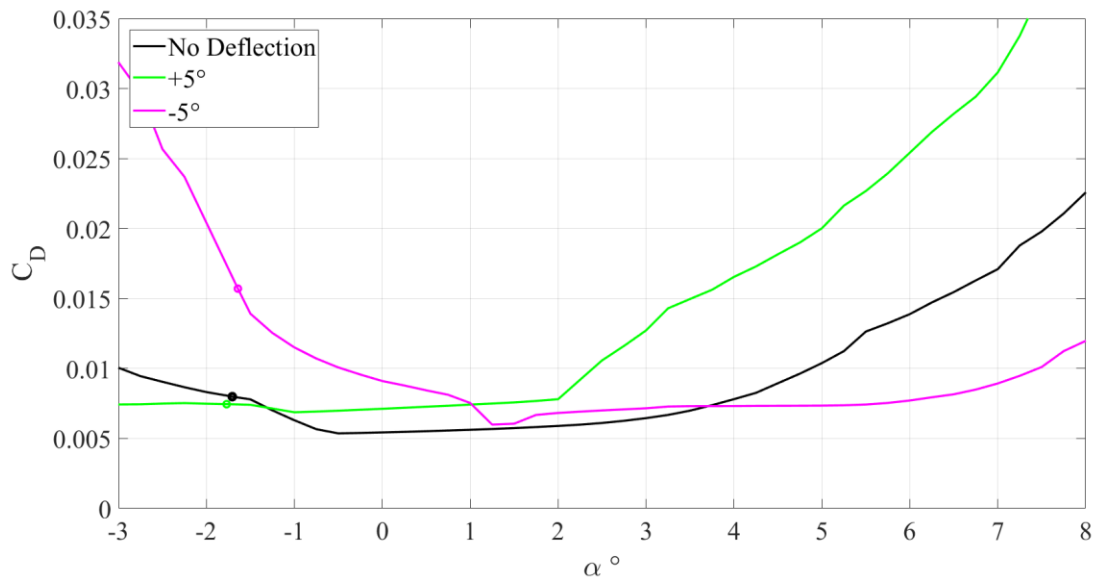


Figure 4.6: Winglet Top Airfoil Parasitic Drag Polar

4.2.2 Camber Effects on Wing Induced Drag

The effect of flap deflection on induced drag for the entire wing was less pronounced than their effect on parasitic drag, so the induced drag for winglet configurations were compared against the winglets with no camber as a percentual, as shown in Figure 4.7. The positive winglet flap deflection produced a 20% increase in induced drag for the low g flight condition over a winglet with no flap deflection. However, the induced drag at the high g flight condition shows a 1% decrease in induced drag, meaning that the winglet with $+5^\circ$ of flap deflection is more efficient at this condition than the winglet with no flap deflection. The -5° winglet deflection produced 10% increase in induced drag at the low lift condition, while at the high g condition, the negative flap deflection produced a 1.3% increase in drag.

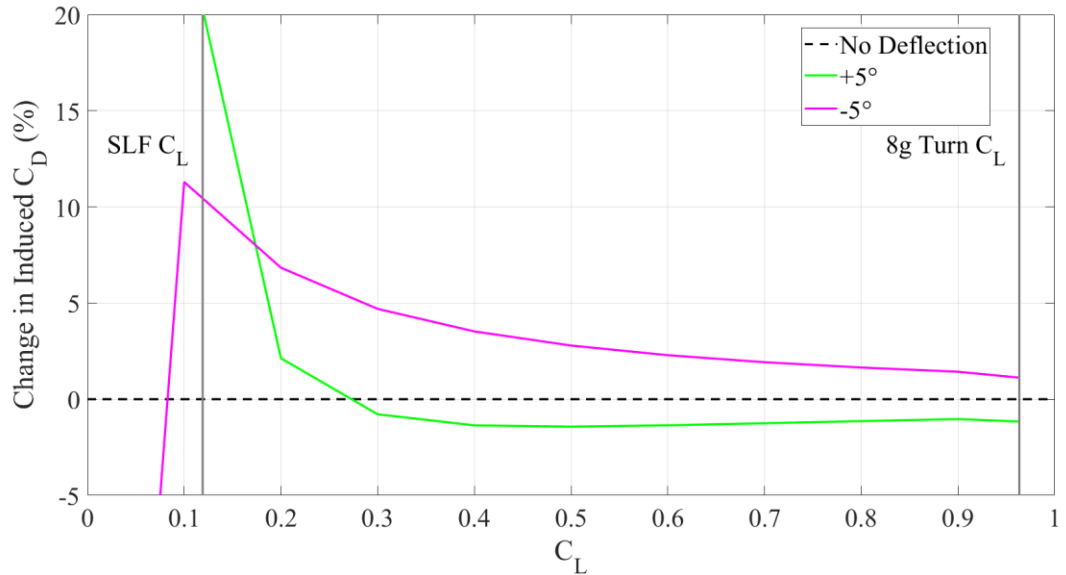


Figure 4.7: Effect of Winglet Flap Deflection on Induced Drag

4.2.3 Camber Effects on Wing Total Drag

These results from the induced drag comparison are replicated in the total drag comparison for the winglet configurations as shown in Figure 4.8. Both winglet flap deflections produced 1.2% more drag than the winglet with no flap deflection at the low g condition. It is clear that a negative flap deflection produces an increase in drag while the positive flap deflection produced a decrease

in drag for most of the range of lift compared to no flap deflection. The discrepancy between the 1% decrease in induced drag and 0.65% decrease in total drag for the $+5^\circ$ flap deflection at the high g condition comes from the increase in parasitic drag at this condition, however the reduction in induced drag was enough to provide a net benefit for this configuration. The effect of the winglet flap deflections on efficiency is shown in Figure 4.9, where no flap deflection produced the highest efficiency for the low g condition and $+5^\circ$ flap deflection produced the highest efficiency for the high g condition.

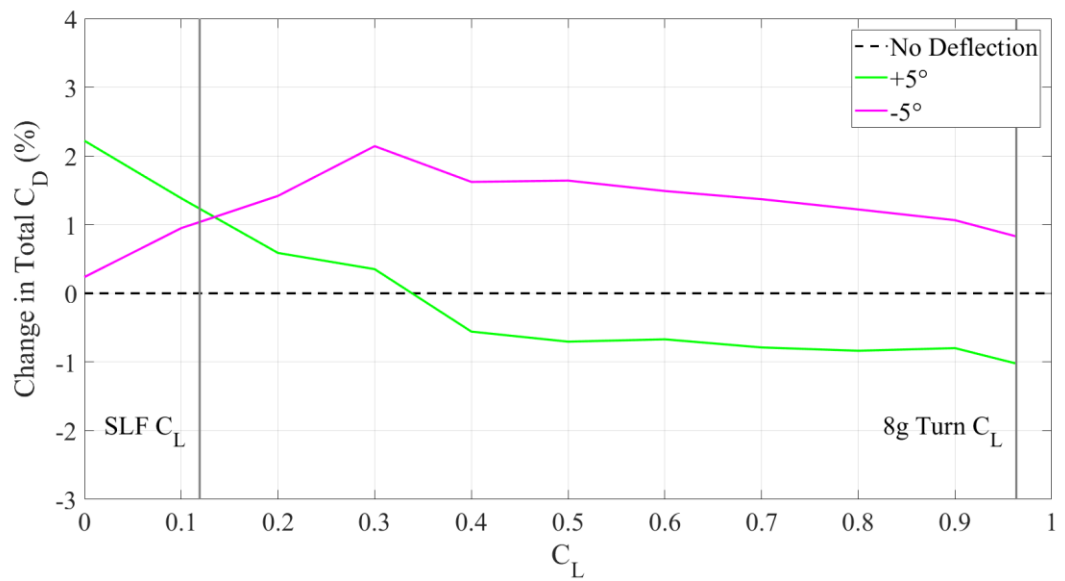


Figure 4.8: Effect of Winglet Flap Deflection on Total Drag

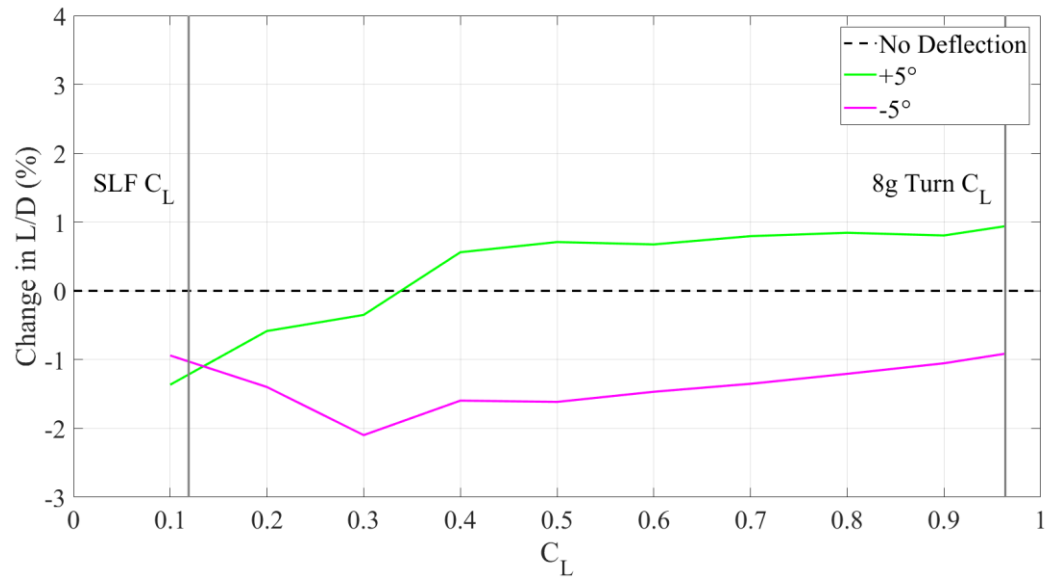


Figure 4.9: Effect of Winglet Flap Deflection on Efficiency

4.3 8g Turn Efficiency

The effect of changing hinge locations and flap deflections for the high lift condition is shown in Figure 4.10, where the percentual difference in efficiency for each configuration is compared to the winglet with no deflection. It should be noted that adding a winglet increases efficiency by 10% compared to a wing with no winglet. The x-axis represents winglet flap deflection in degrees and the y-axis represents the change in wing efficiency compared to a wing with no winglet. Adding camber increases efficiency for positive deflections while removing camber with negative deflections decreases efficiency. Furthermore, there is a more pronounced change in efficiency the closer the hinge is moved to the leading edge of the winglet. Based on these results, it is better to add some positive deflection to the winglet since this will produce more than the 10% gain in efficiency that the original winglet produces. Since there is an upward trend in efficiency with flap deflection, a larger deflection than 5° should produce even higher efficiencies.

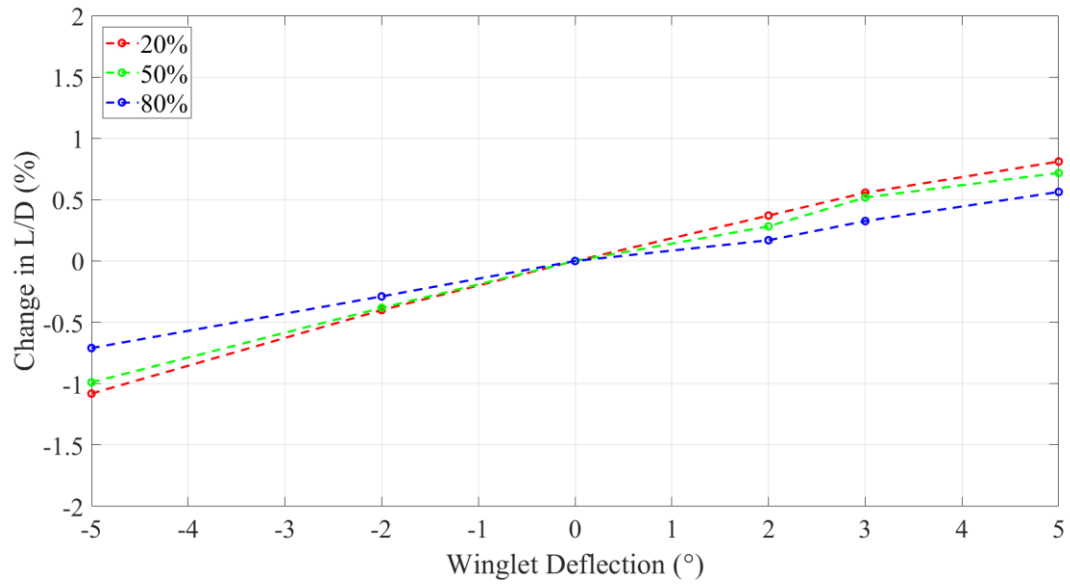


Figure 4.10: Effect of Winglet Camber at High g Turn

A detailed investigation of the winglets' effect on the entire wing's lift and drag distribution was carried out on the 50% chord hinge location for the $+5^\circ$ and -5° flap deflections to explain why positive flap deflections may benefit efficiency at high g conditions over negative or no flap deflection. Based on the wing's lift distribution as seen in Figure 4.11, the positive winglet deflection provides more lift towards the end of the winglet as opposed to the other configurations, up to 4% near the end of the span. This is accompanied by an increase in induced drag towards the wing tip, but less induced drag in the main span of the wing for this configuration as shown in Figure 4.12. This decrease in drag is related to the lower angle of attack needed for the entire wing with the positive winglet deflection, since more of the load for producing the C_L of 0.9634 required to fly at this condition is distributed to the winglet. The negative winglet deflection on the other hand produced less induced drag and lift at the wing tips but more induced drag towards the wing root, which indicates a higher wing angle of attack due to less load carried at the wingtips.

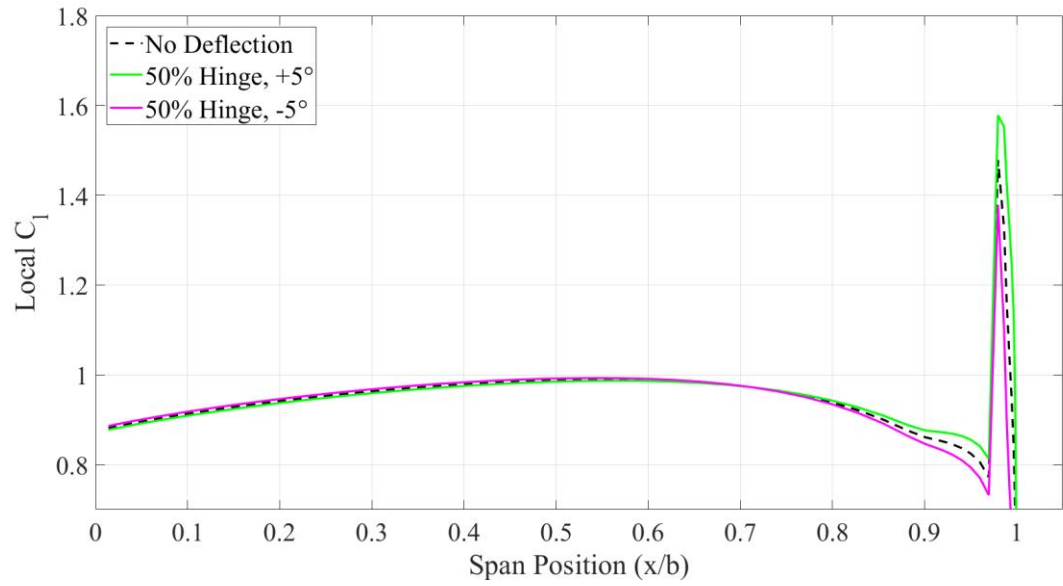


Figure 4.11: Effect of Winglet Flap Deflection on Lift Distribution, High g Condition

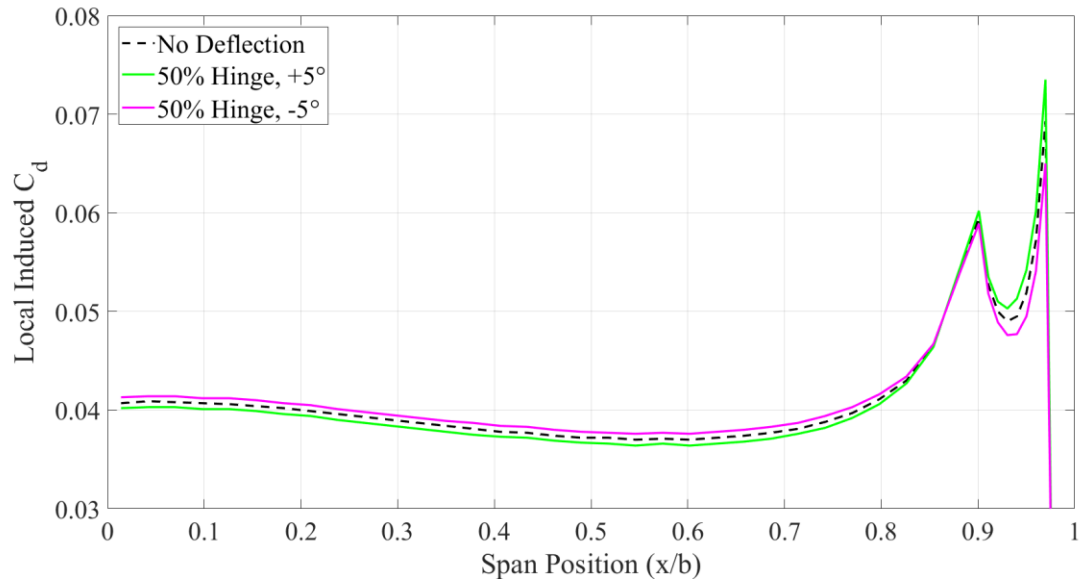


Figure 4.12: Effect of Winglet Flap Deflection on Induced Drag Distribution, High g Condition

It can be seen in Figure 4.13 that the parasitic drag for the positive flap deflection is higher than the other configurations, while the negative flap deflection produces the least parasitic drag. The overall effect this has on total drag is not as large as induced drag, however, as the trend for total drag more closely follows that of induced drag as seen in Figure 4.14, as the scale in magnitude for parasitic drag is 20% of the magnitude of induced drag.

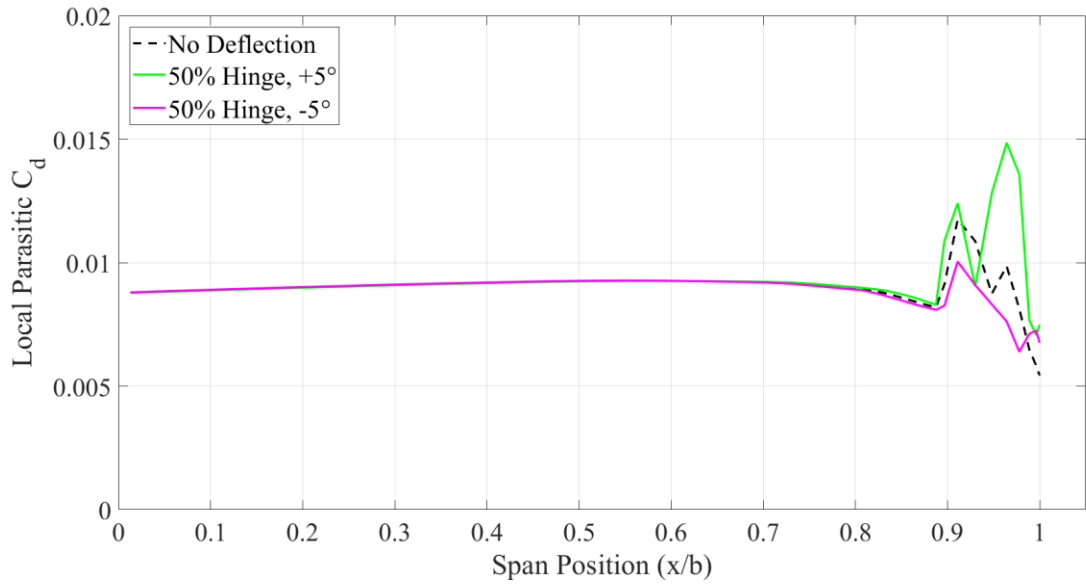


Figure 4.13: Effect of Winglet Flap Deflection on Parasitic Drag Distribution, High g Condition

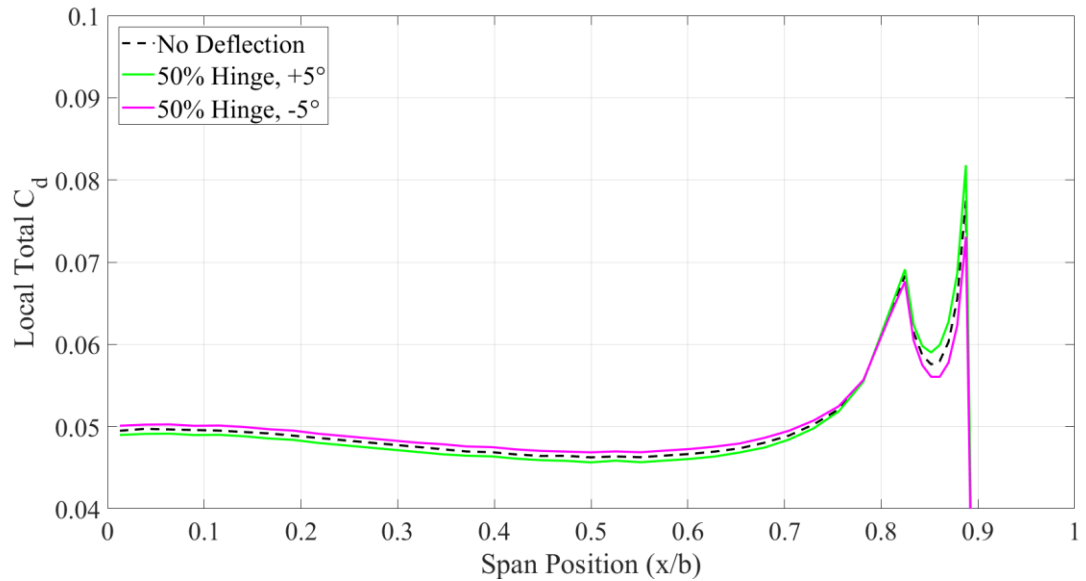


Figure 4.14: Effect of Winglet Flap Deflection on Total Drag Distribution, High g Condition

These figures showed that lift is proportional to drag but increasing winglet camber provides a larger increase in lift proportional to the increase in drag since the positive deflection improved efficiency over a non-deflected winglet. The overall gain or loss in efficiency due to winglet deflection for this condition is ranges between -1.2% and 0.7% for negative and positive deflection respectively; while these values are small, any improvement in efficiency can make the

difference for an air race where a fraction of a second can determine whether an aircraft wins or loses the race.

4.4 Steady Level Flight Efficiency

The percentual differences for different winglet configurations for the low g condition is shown in Figure 4.15. An important note is that adding any winglet reduces the wing efficiency compared to a wing with no winglet due to the additional parasitic drag caused by the increased wetted area of the winglet and the low importance of induced drag for this flight condition. Deflecting the winglet flap by any amount in either direction decreased wing efficiency compared to a winglet with no flap deflection and moving the flap hinge towards the leading edge of the winglet amplifies the flap's effect on efficiency.

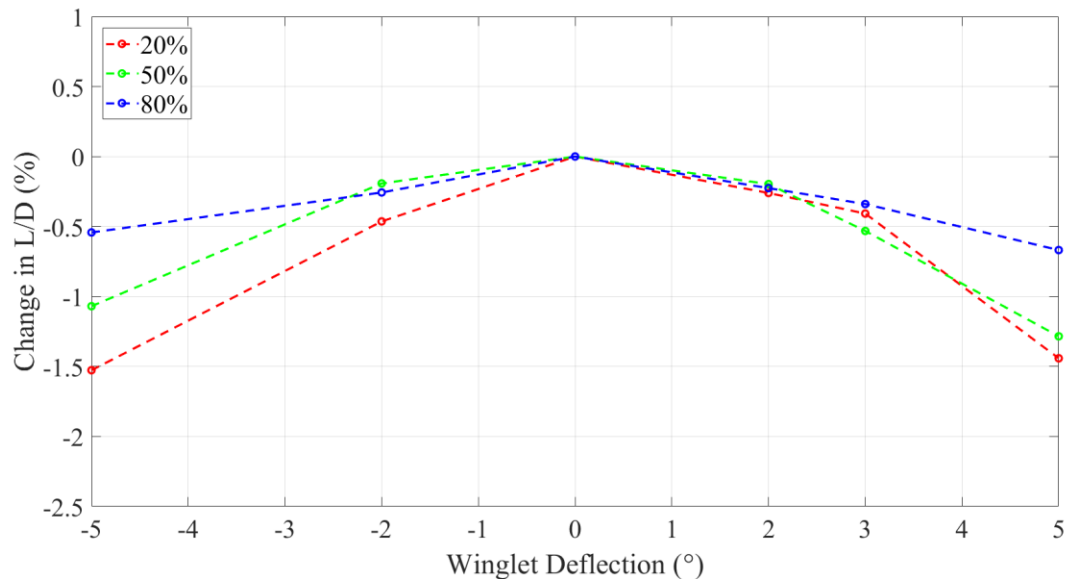


Figure 4.15: Effect of Winglet Camber at Low g Steady Level Flight

This decrease in efficiency for any flap deflection at the low g flight condition can be explained by the spanwise drag production of the wing compared to its lift. Figure 4.16 and Figure 4.17 shows the effect of the winglets on the wing's lift distribution and corresponding induced drag distribution for the low g flight condition. Positive flap deflections provide more lift at the winglets, increasing the induced drag produced over a winglet with no flap deflection. Conversely, negative

flap deflections decrease the loading and the induced drag of the winglets. It should be noted that any winglet deflection does not produce a noticeable change in lift or induced drag for the main span of the wing compared to winglet loading.

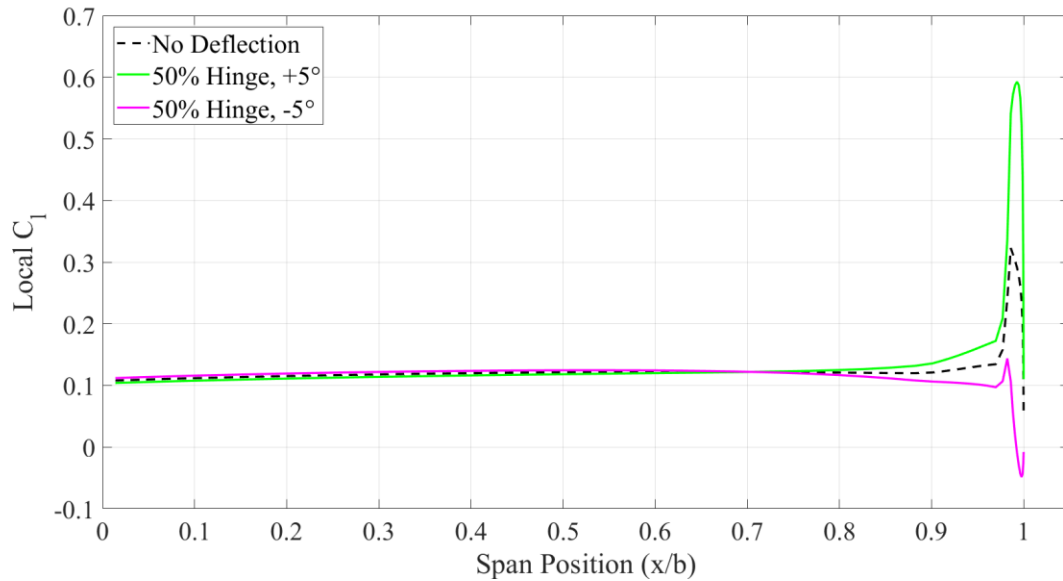


Figure 4.16: Effect of Winglet Flap Deflection on Lift Distribution, Low g Condition

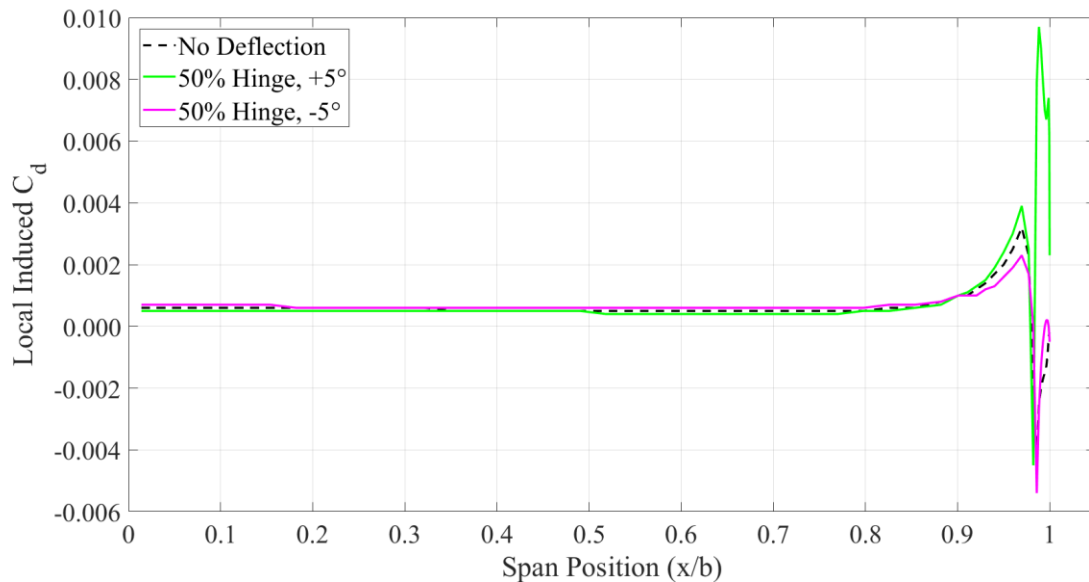


Figure 4.17: Effect of Winglet Flap Deflection on Induced Drag Distribution, Low g Condition

Although the induced drag changes proportionally with lift, the parasitic drag always increases with winglet flap deflection for this condition as shown in Figure 4.18. The discontinuity

in airfoil curvature caused by the hinge and flap deflection causes an increase in parasitic drag for any deflection, with negative deflections causing a larger increase in drag than positive deflections. It can be seen that at the base and top of the winglet, the $+5^\circ$ flap deflection produces less parasitic drag than the winglet with no flap deflection, as referenced earlier by Figures 4.5 and 4.6. However, this deflection still produces more parasitic drag over the rest of the winglet span. This increase in parasitic drag for both positive and negative deflections is much larger in magnitude than induced drag and causes the total drag to increase over the winglet with no deflections, as shown in Figure 4.19.

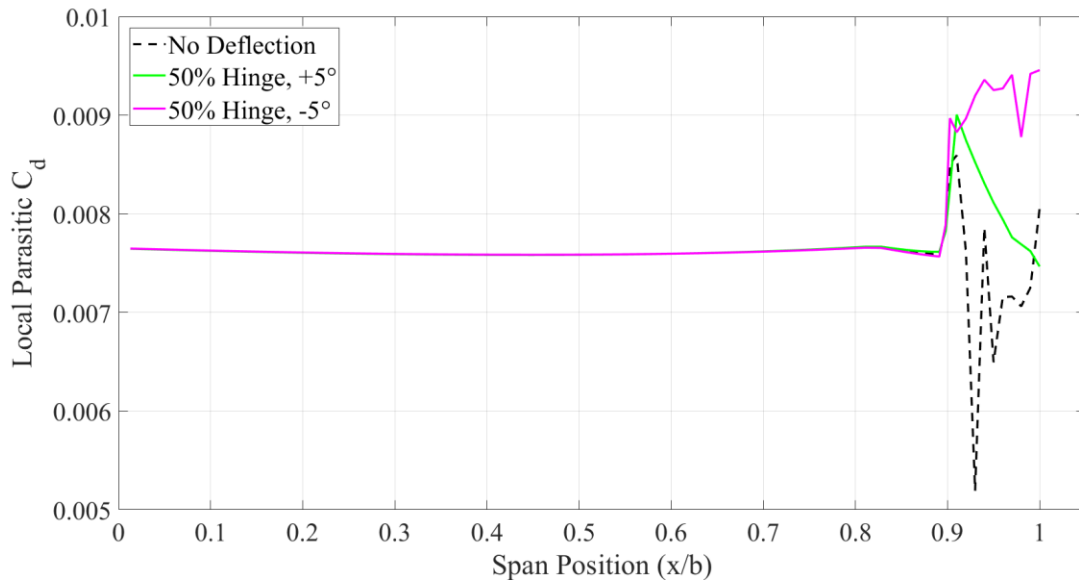


Figure 4.18: Effect of Winglet Flap Deflection on Parasitic Drag Distribution, Low g Condition

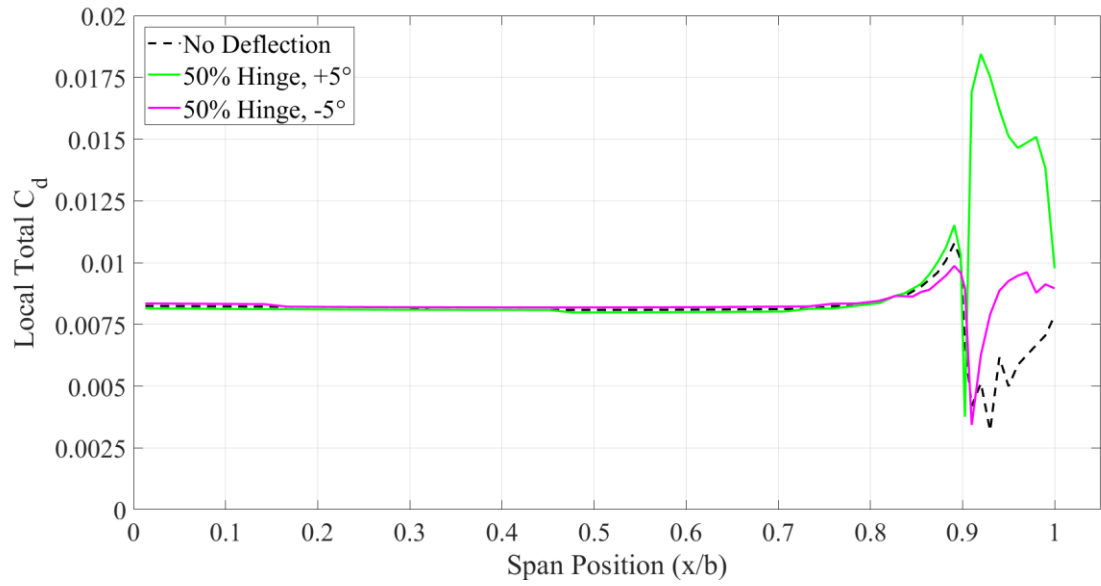


Figure 4.19: Effect of Winglet Flap Deflection on Total Drag Distribution, Low g Condition

Unlike the high g condition, a negative winglet deflection produces a decrease in lift but an increase in total drag compared to a non-deflected winglet, which has the effect of decreasing efficiency. The positive deflection shows an increase in both lift and drag, but the drag increased more than the lift to create a lower efficiency. The behavior of these configurations shows that the most efficient winglet configuration is the base winglet with no flap deflection.

Chapter 5

CONCLUSION

A numerical study of the effect of changing winglet camber on the efficiency for an acrobatic race plane wing was performed using a low-fidelity vortex lattice method. This method was validated against a high-fidelity Reynolds Averaged Navier-Stokes computational fluid dynamics method to determine where the limitations of VLM prevented computation of accurate results. It was found that VLM can produce accurate results for lower lift conditions, but the drag results of VLM increasingly diverged from RANS drag calculations with increasing C_L . However, VLM can be used to quickly test many configurations and optimize a winglet design, from which a wind tunnel model or flight test apparatus can be built to obtain values for efficiency that more reflect the flight conditions seen in reality.

Based on VLM results of the two flight regimes tested, a low g steady level flight condition at 200 knots and an 8g turn at 200 knots, it was shown that positive winglet flap deflections can increase the wing efficiency at the high g condition. For the low g flight condition, it was determined that any deflection in the winglet flap produced more drag, and thus decrease efficiency. Therefore, the most efficient winglet configuration would be the winglet with no flap deflection for this high-speed condition.

In the context of an acrobatic race plane flying through a circuit, the winglets on this plane should be configured to have no change in camber during steady level flight, and introduce positive deflection during high g maneuvers to increase efficiency over an aircraft with static winglets. Although the increase in efficiency that the adaptive camber winglets can offer may be less than 1%, this may provide the edge needed to win a race, where lap times can differ by milliseconds and small mistakes and gains can mean the difference between first and second place.

Chapter 6

FUTURE WORK

Since the increase in parasitic drag due to the plain flap deflection decreased efficiency for the high speed condition, it is of interest to perform the same analysis on the same wing used in this study, but for a flap with no discontinuity in winglet camber curvature. A study using a smooth transition in camber curvature for the winglet would determine if a more complex change in geometry can produce higher efficiencies for this high-speed condition.

Due to the lack of agreement between RANS and VLM drag results for the high g condition, wind tunnel or flight testing should be performed with this adaptive camber winglet at this condition to provide another source of validation, where the results will determine which of the two numerical methods used in this study is more accurate to reality.

Numerical analysis for adaptive camber winglets on a fully modelled aircraft should be attempted to determine the winglets' effect on aircraft efficiency and interaction with the entire body of the aircraft. The ability for VLM to model an aircraft fuselage is limited [17], but RANS or other high-fidelity methods involving domain discretization like large eddy simulation or direct numerical simulation can be used to model and analyze complex geometry.

The winglet used in this study was optimized for high-speed flight, as evidenced by the configuration with no flap deflection producing the highest efficiency. As such, it may be of interest to perform the same type of analysis seen in this study on a winglet designed for a different condition.

REFERENCES

- [1] Whitcomb, Richard T., “A Design Approach and Selected Wind-Tunnel Results at High Subsonic Speeds for Wing-tip Mounted Winglets,” NASA Technical Note D-8260, July 1976
- [2] Daily News Hungary, <https://dailynewshungary.com/red-bull-air-race-2017-results-photos/>
- [3] Jones, R. T., Lasinski, T. A., “Effect of Winglets on the Induced Drag of Ideal Wing Shapes,” NASA Technical Memorandum 81230, Sept. 1980
- [4] Colling, J., “Sailplane Glide Performance and Control Using Fixed and Articulating Winglets,” NASA CR-198579, May 1995
- [5] Rademacher, P. R., “Winglet Performance Evaluation through the Vortex Lattice Method,” *Embry-Riddle Aeronautical University Scholarly Commons*, May 2014
- [6] Chattot, Jean-Jacques, “Low Speed Design and Analysis of Wing/Winglet Combinations Including Viscous Effects,” *Journal of Aircraft*, Vol. 43, No. 2, April 2006
- [7] Maughmer, M. D., “The Design of Winglets for High-performance Sailplanes,” AIAA Paper 2001-2406, 2001
- [8] Azlin, M. A et al., “CFD Analysis of Winglets at Low Subsonic Flow,” *Proceedings of the World Congress on Engineering*, Vol I, July 2011.
- [9] Ursache, Narcis M. et al., “Technology Integration for Active Poly-Morphing Winglets Development,” *Proceedings of SMASIS 2008*, October 2008
- [10] Wang, Chen et al., “Investigating the Benefits of Morphin Wing Tip Devices – A Case Study,” *International Forum on Aeroelasticity and Structural Dynamics*, June 2015
- [11] Vos, R., Gürdal, Z., Abdalla, M., “Mechanism for Warp-Controlled Twist of a Morphing Wing,” *Journal of Aircraft*, Vol. 47, No. 2, March 2010

- [12] De Breuker, R. V. R, Barrett, R., Tiso, P., “Morphing Wing Flight Control via Post-Buckled Precompressed Piezoelectric Actuators,” *Journal of Aircraft*, Vol. 44, No. 4, Jul. 2007, pp. 1060-1068, doi: 10.2514/1.21292
- [13] Lyu, Z., Martins, J. R. R. A., “Aerodynamic Shape Optimization of an Adaptive Morphing Trailing-Edge Wing,” *Journal of Aircraft*, Vol. 52, No. 6, Nov. 2015, pp. 1951-1970, doi: 10.2514/1.C033116
- [14] Park, P. S., Rokhsaz, K., “Effects of a Winglet Rudder on Lift-to-Drag Ratio and Wake Vortex Frequency,” AIAA Paper 2003-4069, June 2003
- [15] Eguea, João Paulo et al., “Study on a Camber Adaptive Winglet,” *Applied Aerodynamics Conference*, AIAA, Atlanta, Georgia, June 2018, doi: 10.2514/6.2018-3960
- [16] Singh, Diwakar et al., “A Multi-Fidelity Approach for Aerodynamic Performance Computations of Formation Flight,” MDPI, June 2018
- [17] Drela, M., Youngren, H., “AVL 3.36 User Primer,” Feb. 2017
- [18] Hough, Gary R., “Lattice Arrangements for Rapid Convergence,” *Vortex Lattice Utilization*, NASA SP-405, May 1976
- [19] Drela, M., Youngren, H., “XFOIL 6.9 User Primer,” Nov. 2001
- [20] Deperrois, André, “Theoretical Limitations and Shortcomings of XFLR5,” June 2019
- [21] van Ingen, J.L., “The eN method for transition prediction. Historical review of work at TU Delft,” AIAA Paper 2008-3830, June 2008
- [22] Kaynak, Unver et al., “Transition Modeling for Low to High Speed Boundary Layer Flows with CFD Applications,” *intechopen*, Jan. 2019, doi: 10.5772/intechopen.83520
- [23] Moran, Jack, “An Introduction to Theoretical and Computational Aerodynamics,” *John Wiley & Sons*, 1984, ISBN: 0-471-47491-4
- [24] Abbott, Ira H., Von Doenhoff, Albert E., “Theory of Wing Sections,” *Dover Publications*, New York, 1959, Standard Book Number: 486-60586-8

- [25] Monsch, Scott, “A Study of Induced Drag and Spanwise Lift Distribution for Three-Dimensional Inviscid Flow Over a Wing,” *Engineering Mechanics Commons*, May 2007
- [26] Anderson, John D., “Fundamentals of Aerodynamics,” Fifth Edition, *McGraw-Hill*, 2010, ISBN: 978-0-07-339810-5
- [27] Siemens, “Force,” *Star CCM+ User Guide*, 2020
- [28] Hall, Nancy, “Navier-Stokes Equations 3-dimensional-unsteady,” NASA, May 2015, <https://www.grc.nasa.gov/www/k-12/airplane/nseqs.html>
- [29] Mohammadi, Bijan, and Pironneau, Olivier, “Analysis of the K-Epsilon Turbulence Model,” Dec. 1993, ISBN: 2-225-84391-0

APPENDIX

Table A1: Airfoil Coordinates

Wing Root		Wingtip		Winglet Base		Winglet Top	
1.00000	0.00000	1.00000	0.00000	1.00000	0.00000	1.00000	0.00000
0.99431	0.00098	0.99501	0.00093	0.99630	0.00073	0.99653	0.00055
0.98567	0.00244	0.98713	0.00239	0.98978	0.00203	0.98977	0.00164
0.97696	0.00393	0.97880	0.00393	0.98187	0.00361	0.98085	0.00311
0.96818	0.00536	0.97004	0.00545	0.97277	0.00544	0.97133	0.00467
0.95937	0.00671	0.96087	0.00687	0.96303	0.00741	0.96181	0.00626
0.95046	0.00797	0.95131	0.00821	0.95306	0.00941	0.95218	0.00786
0.94131	0.00920	0.94140	0.00948	0.94294	0.01148	0.94238	0.00952
0.93188	0.01041	0.93119	0.01069	0.93276	0.01354	0.93257	0.01117
0.92209	0.01162	0.92073	0.01185	0.92253	0.01563	0.92282	0.01281
0.91195	0.01283	0.91003	0.01297	0.91228	0.01774	0.91308	0.01448
0.90151	0.01405	0.89908	0.01406	0.90204	0.01986	0.90337	0.01614
0.89082	0.01526	0.88788	0.01511	0.89180	0.02200	0.89371	0.01779
0.87983	0.01647	0.87647	0.01612	0.88158	0.02413	0.88402	0.01942
0.86845	0.01769	0.86491	0.01710	0.87151	0.02626	0.87433	0.02103
0.85656	0.01890	0.85317	0.01804	0.86144	0.02833	0.86459	0.02265
0.84412	0.02013	0.84127	0.01897	0.85130	0.03041	0.85482	0.02425
0.83120	0.02140	0.82917	0.01986	0.84116	0.03249	0.84509	0.02584
0.81787	0.02268	0.81683	0.02074	0.83104	0.03453	0.83531	0.02740
0.80417	0.02397	0.80431	0.02159	0.82098	0.03655	0.82549	0.02898
0.79018	0.02526	0.79163	0.02241	0.81097	0.03854	0.81572	0.03053
0.77596	0.02654	0.77884	0.02322	0.80095	0.04051	0.80593	0.03205
0.76154	0.02784	0.76600	0.02401	0.79086	0.04249	0.79621	0.03357
0.74700	0.02913	0.75313	0.02478	0.78066	0.04445	0.78646	0.03505
0.73236	0.03039	0.74028	0.02553	0.77041	0.04643	0.77687	0.03648
0.71763	0.03165	0.72747	0.02625	0.76015	0.04838	0.76742	0.03791
0.70285	0.03291	0.71473	0.02694	0.74991	0.05028	0.75779	0.03929
0.68808	0.03418	0.70210	0.02762	0.73966	0.05218	0.74823	0.04070
0.67332	0.03544	0.68967	0.02833	0.72941	0.05405	0.73873	0.04203
0.65857	0.03669	0.67724	0.02921	0.71923	0.05588	0.72914	0.04337
0.64379	0.03797	0.66459	0.03011	0.70913	0.05767	0.71937	0.04469
0.62897	0.03925	0.65178	0.03102	0.69902	0.05940	0.70974	0.04599
0.61410	0.04057	0.63887	0.03195	0.68892	0.06114	0.70024	0.04722
0.59918	0.04189	0.62586	0.03290	0.67889	0.06282	0.69071	0.04843
0.58424	0.04324	0.61277	0.03386	0.66883	0.06448	0.68101	0.04963
0.56926	0.04461	0.59964	0.03483	0.65878	0.06609	0.67121	0.05079
0.55425	0.04599	0.58649	0.03581	0.64876	0.06765	0.66147	0.05189
0.53921	0.04740	0.57331	0.03681	0.63862	0.06919	0.65167	0.05298
0.52417	0.04881	0.56013	0.03782	0.62847	0.07071	0.64184	0.05405
0.50912	0.05023	0.54695	0.03884	0.61835	0.07216	0.63210	0.05505
0.49406	0.05167	0.53378	0.03986	0.60820	0.07354	0.62230	0.05599
0.47901	0.05312	0.52064	0.04088	0.59801	0.07487	0.61251	0.05689
0.46397	0.05456	0.50755	0.04192	0.58781	0.07615	0.60271	0.05776
0.44897	0.05600	0.49446	0.04296	0.57765	0.07738	0.59284	0.05860

0.43401	0.05745	0.48138	0.04400	0.56757	0.07853	0.58318	0.05937
0.41912	0.05887	0.46831	0.04504	0.55746	0.07959	0.57344	0.06011
0.40428	0.06028	0.45523	0.04609	0.54735	0.08061	0.56363	0.06082
0.38954	0.06167	0.44215	0.04714	0.53732	0.08157	0.55371	0.06149
0.37490	0.06302	0.42910	0.04818	0.52736	0.08247	0.54388	0.06213
0.36039	0.06434	0.41607	0.04920	0.51725	0.08329	0.53402	0.06270
0.34604	0.06561	0.40304	0.05024	0.50704	0.08405	0.52409	0.06326
0.33185	0.06682	0.38999	0.05126	0.49678	0.08478	0.51419	0.06379
0.31783	0.06795	0.37698	0.05226	0.48655	0.08545	0.50440	0.06428
0.30400	0.06902	0.36400	0.05325	0.47638	0.08606	0.49457	0.06469
0.29039	0.06999	0.35107	0.05420	0.46623	0.08658	0.48472	0.06506
0.27699	0.07087	0.33818	0.05512	0.45593	0.08703	0.47492	0.06533
0.26382	0.07166	0.32534	0.05601	0.44562	0.08747	0.46504	0.06557
0.25093	0.07235	0.31258	0.05685	0.43548	0.08786	0.45530	0.06585
0.23832	0.07292	0.29990	0.05765	0.42554	0.08815	0.44556	0.06611
0.22604	0.07339	0.28732	0.05838	0.41558	0.08828	0.43576	0.06637
0.21410	0.07376	0.27480	0.05905	0.40545	0.08835	0.42590	0.06658
0.20255	0.07401	0.26239	0.05966	0.39523	0.08838	0.41611	0.06672
0.19143	0.07415	0.25008	0.06019	0.38488	0.08844	0.40638	0.06676
0.18073	0.07416	0.23789	0.06066	0.37461	0.08851	0.39645	0.06677
0.17047	0.07407	0.22583	0.06104	0.36445	0.08852	0.38647	0.06679
0.16069	0.07387	0.21394	0.06135	0.35455	0.08844	0.37665	0.06678
0.15138	0.07356	0.20225	0.06156	0.34454	0.08820	0.36694	0.06668
0.14252	0.07315	0.19078	0.06168	0.33436	0.08790	0.35709	0.06657
0.13412	0.07263	0.17957	0.06169	0.32414	0.08757	0.34722	0.06640
0.12618	0.07201	0.16865	0.06160	0.31401	0.08721	0.33734	0.06618
0.11865	0.07129	0.15806	0.06141	0.30388	0.08675	0.32750	0.06596
0.11153	0.07049	0.14785	0.06109	0.29368	0.08621	0.31776	0.06570
0.10479	0.06962	0.13802	0.06066	0.28343	0.08563	0.30792	0.06536
0.09842	0.06869	0.12862	0.06012	0.27327	0.08500	0.29800	0.06497
0.09240	0.06770	0.11967	0.05947	0.26320	0.08429	0.28811	0.06454
0.08670	0.06666	0.11119	0.05871	0.25310	0.08349	0.27823	0.06406
0.08132	0.06557	0.10317	0.05786	0.24293	0.08262	0.26838	0.06354
0.07623	0.06442	0.09564	0.05694	0.23285	0.08171	0.25852	0.06295
0.07141	0.06323	0.08858	0.05594	0.22287	0.08070	0.24865	0.06232
0.06684	0.06199	0.08199	0.05487	0.21287	0.07960	0.23881	0.06164
0.06252	0.06069	0.07584	0.05375	0.20287	0.07843	0.22900	0.06090
0.05842	0.05935	0.07011	0.05256	0.19297	0.07717	0.21921	0.06009
0.05453	0.05796	0.06477	0.05132	0.18313	0.07582	0.20943	0.05920
0.05084	0.05654	0.05978	0.05004	0.17327	0.07436	0.19965	0.05825
0.04734	0.05506	0.05514	0.04871	0.16343	0.07282	0.18984	0.05722
0.04402	0.05353	0.05081	0.04733	0.15379	0.07121	0.18008	0.05614
0.04088	0.05196	0.04678	0.04591	0.14425	0.06946	0.17041	0.05497
0.03789	0.05035	0.04300	0.04445	0.13471	0.06758	0.16077	0.05370
0.03505	0.04870	0.03948	0.04296	0.12524	0.06560	0.15108	0.05232
0.03237	0.04703	0.03618	0.04143	0.11596	0.06351	0.14140	0.05086
0.02983	0.04532	0.03310	0.03988	0.10681	0.06127	0.13181	0.04931
0.02742	0.04358	0.03021	0.03831	0.09776	0.05890	0.12231	0.04765
0.02515	0.04182	0.02752	0.03672	0.08888	0.05638	0.11284	0.04585
0.02299	0.04005	0.02499	0.03511	0.08014	0.05370	0.10335	0.04391
0.02096	0.03826	0.02263	0.03349	0.07162	0.05089	0.09394	0.04186

0.01903	0.03646	0.02042	0.03187	0.06338	0.04795	0.08467	0.03966
0.01721	0.03466	0.01834	0.03025	0.05547	0.04488	0.07548	0.03729
0.01549	0.03286	0.01641	0.02864	0.04792	0.04167	0.06638	0.03474
0.01387	0.03106	0.01460	0.02703	0.04078	0.03835	0.05743	0.03199
0.01234	0.02926	0.01291	0.02543	0.03413	0.03497	0.04863	0.02904
0.01091	0.02746	0.01133	0.02383	0.02818	0.03167	0.03979	0.02578
0.00957	0.02567	0.00986	0.02225	0.02300	0.02849	0.03168	0.02241
0.00831	0.02388	0.00850	0.02067	0.01853	0.02544	0.02480	0.01921
0.00715	0.02209	0.00724	0.01910	0.01471	0.02261	0.01772	0.01549
0.00607	0.02031	0.00608	0.01753	0.01151	0.02005	0.01118	0.01134
0.00509	0.01853	0.00502	0.01597	0.00886	0.01775	0.00694	0.00820
0.00419	0.01676	0.00407	0.01440	0.00671	0.01560	0.00470	0.00633
0.00339	0.01499	0.00323	0.01284	0.00499	0.01358	0.00319	0.00491
0.00266	0.01324	0.00248	0.01129	0.00361	0.01165	0.00210	0.00374
0.00203	0.01149	0.00184	0.00974	0.00250	0.00984	0.00129	0.00273
0.00148	0.00974	0.00129	0.00821	0.00163	0.00815	0.00070	0.00183
0.00101	0.00801	0.00084	0.00670	0.00096	0.00660	0.00029	0.00103
0.00063	0.00630	0.00049	0.00521	0.00046	0.00518	0.00006	0.00031
0.00035	0.00461	0.00023	0.00374	0.00012	0.00387	-0.00003	-0.00035
0.00014	0.00295	0.00007	0.00230	-0.00009	0.00267	0.00003	-0.00096
0.00003	0.00130	-0.00000	0.00088	-0.00016	0.00158	0.00022	-0.00152
0.00000	-0.00032	0.00002	-0.00053	-0.00010	0.00058	0.00053	-0.00205
0.00006	-0.00194	0.00014	-0.00192	0.00009	-0.00034	0.00094	-0.00255
0.00021	-0.00357	0.00035	-0.00331	0.00040	-0.00116	0.00147	-0.00302
0.00044	-0.00520	0.00064	-0.00470	0.00084	-0.00192	0.00211	-0.00347
0.00075	-0.00686	0.00103	-0.00609	0.00139	-0.00262	0.00286	-0.00390
0.00114	-0.00854	0.00150	-0.00749	0.00205	-0.00326	0.00373	-0.00431
0.00163	-0.01025	0.00205	-0.00890	0.00282	-0.00385	0.00473	-0.00471
0.00220	-0.01199	0.00270	-0.01033	0.00372	-0.00440	0.00587	-0.00510
0.00286	-0.01374	0.00345	-0.01178	0.00474	-0.00491	0.00717	-0.00547
0.00361	-0.01551	0.00429	-0.01325	0.00590	-0.00538	0.00867	-0.00584
0.00445	-0.01729	0.00523	-0.01475	0.00720	-0.00582	0.01039	-0.00621
0.00538	-0.01907	0.00628	-0.01628	0.00868	-0.00623	0.01242	-0.00658
0.00639	-0.02084	0.00745	-0.01784	0.01036	-0.00661	0.01488	-0.00696
0.00749	-0.02263	0.00873	-0.01943	0.01228	-0.00697	0.01803	-0.00738
0.00868	-0.02441	0.01014	-0.02104	0.01452	-0.00731	0.02256	-0.00790
0.00996	-0.02620	0.01165	-0.02266	0.01718	-0.00764	0.03056	-0.00876
0.01133	-0.02800	0.01327	-0.02429	0.02044	-0.00800	0.03833	-0.00964
0.01279	-0.02980	0.01501	-0.02591	0.02455	-0.00845	0.04660	-0.01037
0.01435	-0.03160	0.01686	-0.02752	0.02959	-0.00914	0.05567	-0.01095
0.01600	-0.03340	0.01882	-0.02913	0.03508	-0.00995	0.06555	-0.01147
0.01775	-0.03520	0.02091	-0.03074	0.04102	-0.01065	0.07527	-0.01188
0.01961	-0.03700	0.02314	-0.03235	0.04816	-0.01126	0.08497	-0.01220
0.02157	-0.03880	0.02553	-0.03397	0.05672	-0.01187	0.09477	-0.01242
0.02364	-0.04058	0.02808	-0.03558	0.06580	-0.01240	0.10462	-0.01256
0.02583	-0.04236	0.03081	-0.03718	0.07513	-0.01281	0.11452	-0.01266
0.02814	-0.04412	0.03373	-0.03875	0.08490	-0.01308	0.12444	-0.01272
0.03059	-0.04585	0.03685	-0.04030	0.09495	-0.01330	0.13434	-0.01274
0.03318	-0.04754	0.04019	-0.04181	0.10494	-0.01344	0.14421	-0.01271
0.03591	-0.04921	0.04377	-0.04330	0.11502	-0.01348	0.15414	-0.01264
0.03879	-0.05084	0.04759	-0.04475	0.12525	-0.01347	0.16413	-0.01259

0.04183	-0.05244	0.05168	-0.04617	0.13555	-0.01347	0.17410	-0.01253
0.04503	-0.05400	0.05607	-0.04754	0.14582	-0.01345	0.18397	-0.01244
0.04840	-0.05552	0.06078	-0.04886	0.15605	-0.01336	0.19387	-0.01230
0.05196	-0.05698	0.06583	-0.05014	0.16639	-0.01320	0.20384	-0.01213
0.05571	-0.05840	0.07125	-0.05138	0.17684	-0.01301	0.21380	-0.01194
0.05966	-0.05977	0.07707	-0.05256	0.18734	-0.01280	0.22377	-0.01174
0.06383	-0.06110	0.08331	-0.05369	0.19783	-0.01257	0.23374	-0.01154
0.06823	-0.06238	0.08999	-0.05475	0.20832	-0.01231	0.24369	-0.01134
0.07287	-0.06360	0.09715	-0.05574	0.21886	-0.01203	0.25366	-0.01111
0.07778	-0.06478	0.10478	-0.05666	0.22941	-0.01175	0.26363	-0.01087
0.08296	-0.06591	0.11289	-0.05750	0.23995	-0.01145	0.27359	-0.01062
0.08844	-0.06699	0.12147	-0.05825	0.25049	-0.01114	0.28353	-0.01037
0.09423	-0.06802	0.13051	-0.05889	0.26103	-0.01082	0.29346	-0.01013
0.10036	-0.06898	0.14000	-0.05942	0.27156	-0.01050	0.30339	-0.00987
0.10684	-0.06990	0.14992	-0.05984	0.28211	-0.01017	0.31334	-0.00961
0.11370	-0.07075	0.16022	-0.06015	0.29261	-0.00982	0.32330	-0.00936
0.12095	-0.07152	0.17087	-0.06034	0.30306	-0.00946	0.33319	-0.00911
0.12860	-0.07222	0.18186	-0.06042	0.31346	-0.00911	0.34291	-0.00882
0.13669	-0.07280	0.19313	-0.06041	0.32374	-0.00875	0.35261	-0.00856
0.14523	-0.07329	0.20464	-0.06029	0.33399	-0.00840	0.36247	-0.00826
0.15423	-0.07367	0.21638	-0.06007	0.34430	-0.00805	0.37219	-0.00800
0.16369	-0.07395	0.22832	-0.05977	0.35458	-0.00771	0.38183	-0.00771
0.17362	-0.07411	0.24040	-0.05939	0.36485	-0.00735	0.39147	-0.00745
0.18401	-0.07417	0.25262	-0.05892	0.37523	-0.00699	0.40121	-0.00717
0.19484	-0.07412	0.26496	-0.05839	0.38567	-0.00663	0.41108	-0.00689
0.20610	-0.07394	0.27740	-0.05779	0.39616	-0.00627	0.42094	-0.00663
0.21779	-0.07365	0.28994	-0.05713	0.40659	-0.00590	0.43062	-0.00634
0.22984	-0.07326	0.30254	-0.05640	0.41696	-0.00553	0.44023	-0.00609
0.24223	-0.07276	0.31526	-0.05561	0.42732	-0.00516	0.44982	-0.00581
0.25492	-0.07214	0.32805	-0.05478	0.43772	-0.00480	0.45942	-0.00554
0.26790	-0.07142	0.34092	-0.05390	0.44819	-0.00442	0.46903	-0.00528
0.28115	-0.07061	0.35385	-0.05299	0.45865	-0.00404	0.47863	-0.00500
0.29461	-0.06970	0.36684	-0.05204	0.46896	-0.00365	0.48823	-0.00472
0.30830	-0.06869	0.37990	-0.05107	0.47909	-0.00327	0.49789	-0.00447
0.32219	-0.06760	0.39300	-0.05008	0.48913	-0.00289	0.50774	-0.00416
0.33627	-0.06645	0.40616	-0.04906	0.49915	-0.00252	0.51748	-0.00390
0.35052	-0.06522	0.41934	-0.04804	0.50922	-0.00214	0.52713	-0.00361
0.36493	-0.06394	0.43255	-0.04701	0.51941	-0.00176	0.53683	-0.00335
0.37947	-0.06261	0.44577	-0.04598	0.52977	-0.00137	0.54669	-0.00305
0.39415	-0.06123	0.45898	-0.04494	0.54017	-0.00098	0.55644	-0.00279
0.40895	-0.05984	0.47218	-0.04390	0.55049	-0.00060	0.56629	-0.00249
0.42381	-0.05843	0.48536	-0.04288	0.56079	-0.00021	0.57625	-0.00219
0.43874	-0.05699	0.49850	-0.04185	0.57109	0.00017	0.58619	-0.00189
0.45372	-0.05554	0.51160	-0.04083	0.58131	0.00055	0.59596	-0.00161
0.46875	-0.05410	0.52469	-0.03983	0.59146	0.00091	0.60576	-0.00133
0.48380	-0.05266	0.53776	-0.03882	0.60169	0.00128	0.61557	-0.00104
0.49885	-0.05121	0.55083	-0.03783	0.61207	0.00164	0.62521	-0.00077
0.51389	-0.04978	0.56392	-0.03684	0.62251	0.00201	0.63481	-0.00051
0.52892	-0.04836	0.57702	-0.03586	0.63302	0.00238	0.64441	-0.00022
0.54394	-0.04695	0.59014	-0.03489	0.64355	0.00275	0.65403	0.00004
0.55896	-0.04555	0.60324	-0.03394	0.65405	0.00310	0.66375	0.00031

0.57397	-0.04416	0.61630	-0.03299	0.66455	0.00343	0.67362	0.00057
0.58899	-0.04281	0.62930	-0.03206	0.67503	0.00376	0.68339	0.00084
0.60403	-0.04146	0.64221	-0.03114	0.68550	0.00408	0.69317	0.00111
0.61908	-0.04013	0.65501	-0.03025	0.69588	0.00437	0.70310	0.00137
0.63411	-0.03880	0.66768	-0.02937	0.70626	0.00466	0.71291	0.00161
0.64913	-0.03750	0.68015	-0.02850	0.71668	0.00494	0.72261	0.00186
0.66415	-0.03621	0.69239	-0.02767	0.72706	0.00520	0.73225	0.00207
0.67916	-0.03494	0.70469	-0.02702	0.73731	0.00545	0.74197	0.00232
0.69413	-0.03367	0.71722	-0.02636	0.74747	0.00566	0.75185	0.00253
0.70906	-0.03239	0.72992	-0.02568	0.75756	0.00584	0.76164	0.00275
0.72393	-0.03112	0.74269	-0.02498	0.76769	0.00603	0.77152	0.00292
0.73872	-0.02984	0.75550	-0.02425	0.77797	0.00620	0.78144	0.00311
0.75339	-0.02856	0.76831	-0.02350	0.78829	0.00634	0.79136	0.00329
0.76791	-0.02727	0.78108	-0.02273	0.79870	0.00644	0.80126	0.00345
0.78229	-0.02597	0.79376	-0.02194	0.80913	0.00652	0.81113	0.00359
0.79646	-0.02468	0.80630	-0.02114	0.81957	0.00656	0.82087	0.00372
0.81038	-0.02339	0.81863	-0.02032	0.82996	0.00660	0.83068	0.00382
0.82400	-0.02210	0.83071	-0.01948	0.84032	0.00661	0.84059	0.00392
0.83725	-0.02081	0.84247	-0.01862	0.85061	0.00658	0.85046	0.00397
0.85007	-0.01955	0.85402	-0.01775	0.86096	0.00651	0.86040	0.00400
0.86238	-0.01831	0.86544	-0.01684	0.87131	0.00638	0.87026	0.00402
0.87412	-0.01708	0.87669	-0.01590	0.88169	0.00623	0.88011	0.00401
0.88536	-0.01586	0.88785	-0.01493	0.89189	0.00607	0.88994	0.00397
0.89626	-0.01465	0.89892	-0.01391	0.90207	0.00582	0.89981	0.00387
0.90695	-0.01342	0.90980	-0.01285	0.91231	0.00552	0.90968	0.00377
0.91751	-0.01218	0.92044	-0.01175	0.92258	0.00517	0.91954	0.00364
0.92791	-0.01091	0.93088	-0.01061	0.93274	0.00478	0.92928	0.00343
0.93811	-0.00961	0.94112	-0.00942	0.94291	0.00430	0.93899	0.00318
0.94805	-0.00829	0.95109	-0.00816	0.95301	0.00377	0.94869	0.00288
0.95775	-0.00693	0.96070	-0.00683	0.96286	0.00319	0.95859	0.00251
0.96722	-0.00551	0.96992	-0.00542	0.97242	0.00253	0.96841	0.00210
0.97646	-0.00400	0.97872	-0.00391	0.98139	0.00183	0.97809	0.00161
0.98548	-0.00247	0.98709	-0.00237	0.98943	0.00112	0.98763	0.00098
0.99429	-0.00098	0.99501	-0.00093	0.99620	0.00042	0.99612	0.00032
1.00000	0.00000	1.00000	0.00000	1.00000	0.00000	1.00000	0.00000